Anion arrangement and H^- conductivity in layered perovskite-type oxyhydrides Ba_2MHO_3 (M = Sc, Y)

by

Haq Nawaz

A thesis submitted for the degree of

Doctor of Philosophy

Department of Structural Molecular Science

School of Physical Sciences

The Graduate University for Advanced Studies, SOKENDAI

August 2020

Table of Contents

Chapter 1

Introduction

1.1 Ion conduction in solids

While electrical conduction in solids is basically caused by the mobility of electrons and holes as in the case of metal and semiconductors, some special solids exhibit ionic conduction with conductivity values as high as those of aqueous electrolyte solutions or molten salts. Such materials have special crystal structures with open tunnels or layers which facilitate the movement of ions. The history of ionic conduction in solids dates back to 1834 when Michael Faraday discovered the motion of ions in Ag_2S and PbF_2. Later, Walther Nernst made significant contribution by driving the famous Nernst equation and detected the ionic conduction in doped zirconia. The materials allowing fast ionic diffusion were termed as solid electrolytes or superionic conductors. Takehiko Takahashi in 1967 coined a term Solid state ionics for this particular field of science which deals with the ions in motion in solids and their uses.[1,2] In recent decades, ion conducting materials have got pronounced attention due to possible applications in gas sensors, fuel cells and as electrolytes in batteries.[3–5]

Compared to solids like NaCl or MgO, which have low ionic conductivities, solid electrolytes have ionic conductivities which increase as a function of temperature. Fast ionic conduction has been investigated in a variety of materials. With respect to morphology, the ion conducting materials may be classified as crystalline, amorphous (or glassy), and organic polymer materials. Nano and microcomposite materials are recent additions.[1] Other classifications can be based on type of mobile ions, the dimensionality of conduction pathways and device application.

For crystalline solids, certain conditions need to be satisfied to allow significant ionic diffusion.

a. A high career density, a large number of the ions of one species should be mobile. Career density can be increased by aliovalent doping.
b. For the mobile ions, a large number of empty sites should be available to jump from one position to another. This is prerequisite of (a), as the ions can be mobile only if there are empty sites available for them to occupy.

c. The potential energy difference between empty and occupied sites should be minimum and the activation barrier for jumping between neighboring sites should be low.
d. The structure with high dimensionality of conduction pathways.[5,6]

1.2 Charge carriers for ionic conduction

Based on charge, the fast mobile ions can be categorized into anionic charge carries and cationic charge carries. The characteristics of ionic species such as charge, polarizability and ionic size play a vital role for fast ionic diffusion. Small, highly polarizable and monovalent ionic species are associated with higher ionic conductivities.

Among the cationic conductors, monovalent ionic species such as Ag^{+}, Na^{+}, Cu^{+}, Li^{+}, and H^{+} are more suited for superionic conduction. The highly charged ions despite their smaller ionic size are bound more strongly to the corresponding anions rendering the diffusion of cations very difficult. Nevertheless, Mg^{2+} or some other higher valent charge careers do exist. On the other hand, anions in general are larger in size compared to cations. Therefore, most of the anion conductors do not exhibit high ionic conductivities at ambient temperature. Anion charge carriers until recently were confined to O^{2-}, F^{-} and Cl^{-} ions. Hydride ion is the recent addition to this family.[2,7–10] Table 1.1 lists some common charge carriers and solid state materials which allow the relevant ionic conduction along with ionic conductivities.

Table 1.1 Typical ion conducting solids [2,7]

Mobile Ion	Material	Ion conductivity (S/cm)
H^+	$H_3PW_{12}O_{40}.29H_2O$[11] $CsHSO_4$[12] $BaCe_{0.85}Yb_{0.15}O_{3-\delta}$[13]	σ_{H^+} = 2.0 ×10^{-1} (25°C) = 8 × 10^{-3} (160°C) = 7 × 10^{-4} (300°C)
Li^+	$Li_{10}GeP_2S_{12}$ (LGPS)[14] $La_{0.34}Li_{0.51}TiO_{2.94}$(LLT)[15] $Li_{14}Zn(GeO_4)_4$[16] $Li_{3x}La_{(2/3)-x}TiO3$ (x = 0.11)[15,17]	σ_{Li^+} = 1.2 × 10^{-2} (25°C) = 1 × 10^{-3} (25°C) = 1.3 × 10^{-3} (300°C) = 1 × 10^{-3} (25°C)
Na^+	$Na_2O.11Al_2O_3$[18] $Na_3Zr_2Si_2PO_{12}$[19]	σ_{Na^+} = 2 × 10^{-1} (300°C) = 3 × 10^{-1} (300°C)
Mg^{2+}	$MgZr_4(PO_4)_6$[20]	$\sigma_{Mg^{2+}}$= 3 × 10^{-3} (800°C)
Cu^+	α-CuI[21] $7CuBr.C_6H_{12}N_4CH_2Br$[21] $RbCu_4Cl_3I_2$[22,23]	σ_{Cu^+} = 10^{-1} (450°C) = 2.1 × 10^{-1} (20°C) = 3.4 × 10^{-1} (25°C)
Ag^+	α-AgI[24] $RbAg_4I_5$[24] $Ag_6I_4WO_4$[25]	σ_{Ag^+} = 1.6 (200°C) = 2.7 × 10^{-1} (25°C) = 4.7 × 10^{-2} (25°C)
O^{2-}	$(ZrO_2)_{0.9}(Y_2O_3)_{0.1}$[26] $(Bi_2O_3)_{0.75}(Y_2O_3)_{0.25}$[27] $La_{0.8}Sr_{0.2}Ga_{0.8}Mg_{0.2}O_{3-x}$[28]	$\sigma_{O^{2-}}$ = 2.0 × 10^{-2} (800°C) = 8 × 10^{-2} (600°C) = 3.5 × 10^{-1} (750°C)
F^-	β -$PbSnF_4$[29] β-PbF_2[30] $Bi_{0.9}K_{0.1}F_{2.8}$[31]	σ_{F^-} = 2.5 ×10^{-2} (25°C) = 1 × 10^{-4} (100°C) = 7 ×10^{-4} (25°C)
Cl^-	$PbCl_2$(+3%KCl)[32] $SnCl_2$[33]	σ_{Cl^-} = 3 ×10^{-3} (300°C = 2 × 10^{-2} (200°C)

1.3 Hydride-ion conductors

Hydride ion is a promising charge carrier for fast ionic conduction due to its attractive features such as an appropriate size which is similar to fluorite (F^-) and oxide ions(O^{2-}), large polarizability and compressive nature.[9,10,34]. Hydride ion shows strong reducing properties (H_2/H^- = -2.25V) which are comparable to Mg/Mg^{2+}(-2.36V).[10] In addition, comparted to the other anionic charge carriers, hydride ion offers two redox reactions, therefore hydride ion diffusion can be exploited to form energy storage/conversion devices with higher energy density.

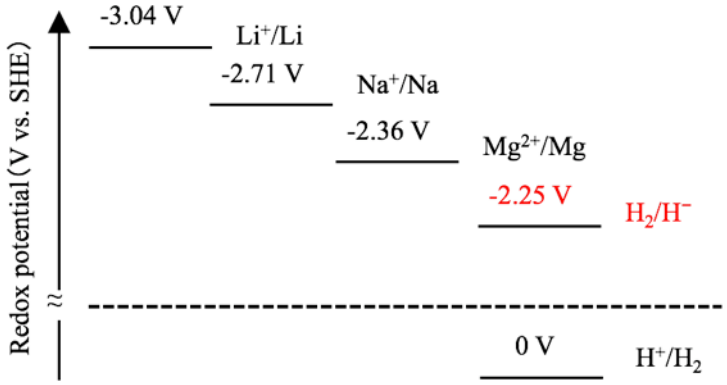

Figure 1.1 Standard redox potential of typical charge carriers

1.3.1 Binary metal hydrides

Hydride ion conduction was initially reported in binary metal hydrides (AeH_2) of alkaline earth metals such as Ba, Ca and Sr.[9,35,36] These metal hydrides although show high hydride ion conductivities but in comparison to metal oxides which have a range of stoichiometries and structural variations, metal hydrides are mostly confined to binary hydrides. Thus, it is difficult to tailor the H^- content as well as the conductivity in metal hydrides. Additionally, metal hydrides are strongly reducing in nature which limit their use for practical applications which require stability in both oxidation and reduction processes.[37]

1.3.2 Oxyhydrides

Oxyhydrides belong to the class of inorganic materials in which oxide and hydride ions share the anionic sublattices. In contrast to metal hydrides, oxyhydrides can exist in variety of structures ranging from Mayenite ($[Ca_{24}Al_{28}O_{64}]^{4+}\cdot 4H^-$)[38,39], perovskite $ATiO_{3-x}H_x$ (A = Ba, Sr, Ca)[40,41] , fluorite $LnH_{3-2x}O_x$ (Ln = La, Ce, Nd, Pr)[34,42,43] to Ruddlesden -Popper

layered perovskites $(A')_2(A)_{n-1}B_n(OH)_{3n+1}$.[44–47] The advances in synthesis techniques, such as the development of topochemical reactions to reduce parent oxide into an oxyhydride as well as the direct synthesis technique under high pressure has led to development of various new oxyhydrides with exciting properties.[48]

Oxyhydrides exhibit several interesting chemical and physical properties such as hydride exchange and electronic conductivity followed by semiconductor to metallic transition in alkali earth titanates[49], insulator to metal transition as a result of π-blocking effect caused by hydride ions in $SrVO_2H$[50], room temperature antiferromagnetic ordering in $LaSrCoO_3H_{0.7}$[44], Catalysts for ammonia synthesis[51] and pure hydride ion conductivity in oxyhydrides like $La_{2-x-y}Sr_{x+y}LiH_{1-x+y}O_{3-y}$ (LSLHO).[10]

1.4 Perovskite structure

The mineral $CaTiO_3$, with an orthorhombic crystal structure was named perovskite after Russian mineralogist Aleksevich Petrovski. Perovskite constitutes a family of minerals with general formula ABX_3. The cation A is in nine coordination, usually a large cation with low valency whereas the B cation is surrounded by six anions and is often highly valent medium-sized cation and X represents the anion. Apart from natural minerals several synthetic perovskites are known which include oxides, nitrides, and oxynitrides. $SrTiO_3$ adopts the ideal or aristotype perovskite structure at room temperature with space group *Pm3-m* (221). The structure consists of corner shared BX_6 octahedra in a three dimensional network where *B-X-B* bond angle is 180° ideally. The structure can be visualized as either A or B cation at the center.[52]

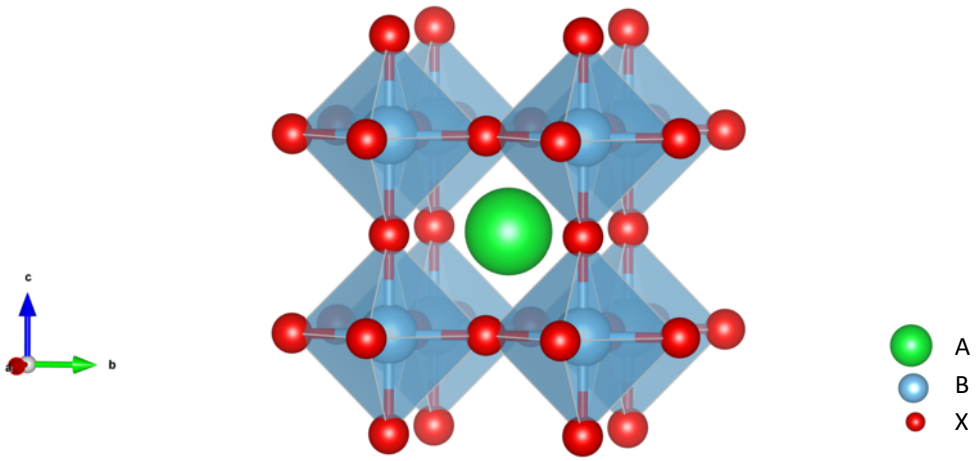

Figure 1.2 Ideal perovskite crystal structure showing corner shared BX_6 octahedra and A cation at the center

The size of the unit cell depends on the *B*-*X* bond length $R_{B\text{-}X}$, the unit cell parameter *a* is twice this distance. The face diagonal is twice the *A*-*X* bond length $R_{A\text{-}X}$. Goldschmidt defined the relationship between these two parameters as tolerance factor *t* given by the equation 1.1 below

$$t = \frac{(r_A + r_X)}{\sqrt{2}(r_B + r_X)} \tag{1.1}$$

Where r_A, r_B and r_X are the ionic radius of the *A*, *B* and *X* respectively in appropriate coordination geometries. The relationship elucidates the likelihood of a pair of cations to form a perovskite structure. For tolerance factor with values $0.9 \leq t \leq 1$, corresponds to cubic geometry, whereas if $t > 1$, hexagonal packing of ABX_3 layers is preferred. For *t* values ranging between 0.71 - 0.9, crystal structures with symmetries lower than cubic are formed. [53,54]

1.5 Ruddlesden-Popper layered structures

When the slabs of the perovskite layers are stacked with rock salt layers, Ruddlesden-Popper (RP) structures are formed. A general formula $A_{n+1}B_nX_{3n+1}$ defines the RP structure with n values ranging between 1-3. When n = 1, the 1st member of this family with K_2NiF_4 type structure is formed which consists of single slabs of ABX_3. The structure is built of successive rock slat (KF) layers which are separated by NiF_2 sheets in sequence … KF, KF, NiF_2 …. Ideally, K_2NiF_4 phase is tetragonal with $a = b \approx a_p$, $c \approx 3.5a_p$ and vector $(\mathbf{a}_p + \mathbf{b}_p)/2$ defines the displacement between neighboring slabs, where $\mathbf{a}_p$ and $\mathbf{b}_p$ are the ideal cubic unit cell vectors.

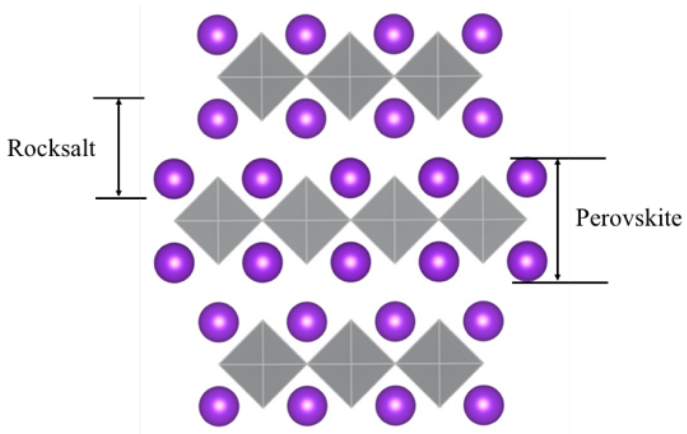

Figure 1.3 Stacking of perosvkite and rock salt layers in ideal K_2NiF_4 structure

Although, K_2NiF_4 typically crystallizes in tetragonal geometry with *I*4/*mmm* crystal structure, the symmetry of the phases may be lowered due to several factors which include, octahedral tilting and distortions and ordering of anions or cations when A, B and X sites are doped with isovalent or aliovalent ions. Higher members of RP series (n = 2,3) are formed by increasing the perovskite slab thickness.[52]

1.5.1 Ionic diffusion in layered oxides

The A_2BO_4 systems are of particular interest for electrochemical energy applications as their oxygen surface exchange kinetics and oxygen diffusion are higher in comparison to the simple ABO_3 perovskite oxides. The adjustment of two different structural units i.e. AO and BO_3 in the lattice of A_2BO_4 system results in strong anisotropic diffusion properties. As already mentioned, B cation is surrounded by six oxide anions, but the B-O bond lengths can vary because of Jahn-Teller distortions caused by the B cations. This leads to two different type of bonds in the BO_6 octahedra called "apical" and "equatorial". The interstitial sites are located in the AO layers where excess oxygen can be placed as a defect or oxygen vacancies can be created by appropriate doping. The oxide ion transport properties are strongly influenced by oxide ion interstitials or vacancies.[55, 56] A fundamental understanding of the oxide ion migration in the A_2BO_4 systems could provide a gateway to design RP type layered oxyhydrides with potential hydride ion conductivity.

1.5.2 Site selectivity in mixed anion materials

In contrast to the layered oxides, the mixed anion systems with $B(O/X)_6$ octahedra X = F^-, Cl^-, Br^-, O^{2-}, S^{2-}, N^{3-} and H^- offer anions to choose preference between apical and equatorial positions. While larger anions such as S^{2-} and Cl^- prefer specific sites when stacked with O^{2-} ion, the small size difference between H^-, N^{3-}, O^{2-} and F^- results in both anion ordered and disordered mixed anion materials. Fuertes *et. al.* described the validity of Pauling's 2nd crystal rule to predict the distribution of anions in mixed oxyanion systems. According to the rule the highly charged anions should occupy positions close to highly charged cations and vice versa. In a layered Ruddlesden-Popper structure, the apical and equatorial sites have different cationic environments. The apical site is surrounded by one *B*-site cation and five *A*-site cations, whereas there are two *B*-site cations and four *A*-site cations surrounding the equatorial site. As mentioned earlier, *B*-site cations (e.g., B^{3+}, B^{4+}) are highly charged compared

to A site cations, consequently, the lower-charged anions such as fluoride occupy the apical sites, and highly charged anions such as nitride tends to occupy the equatorial sites. [57]

This simple electrostatic rule serves as a useful guideline to predict the site selectivity in mixed oxyanion systems, however, for systems with other issues such as size (chloride, bromide and sulfide) or with more covalently bonded anions, the deviations do exist. [58]

1.6 Layered oxyhydrides $La_{2-x-y}Sr_{x+y}LiH_{1-x+y}O_{3-y}$

$La_{2-x-y}Sr_{x+y}LiH_{1-x+y}O_{3-y}$ (LSLHO) is the 1st layered oxyhydride which purely manifested hydride ion conduction. In LSLHO, the highly charged O^{2-} anion occupy positions close to highly charged cations i.e. Sr^{2+} and La^{3+} and vice versa which is in accordance with Pauling's 2nd crystal rule. The incorporation of highly electropositive cations helped to prevent the charge donation by hydride ions thus stabilizing the oxyhydride.

The crystal structure of LSLHO as layered perovskite, typically consists of perovskite and rock salt layers stacked along *c* axis. The 1st member of the series La_2LiHO_3 crystallized in orthorhombic space group with a stoichiometric composition whereas its tetragonal variant $La_2Li(O_{1.21}H_{0.53}\square_{0.26})O_2$ showed disordered anion arrangement in the equatorial plane. Aliovalent doping of Sr for La at A site helped to increase the hydride ion content. $LaSrLiH_2O_2$ consisted of alternate tetragonal $(LiH_2)^-$ and $(LaSrO_2)^+$ layers stacked along the *c*-axis. Further increase of hydride ion content resulted in Sr_2LiH_3O in which additional hydride ion occupied the positions in rock salt layers.

The hydride ion conductivity increased linearly with increase in carrier concentration and highest conductivity of 3.2×10^{-5} S/cm is shown by Sr_2LiHO_3 at 300° C. The structure turnability of layered perovskite was further exploited by introducing anionic vacancies to facilitate the hydride diffusion. The composition $La_{0.6}Sr_{1.4}LiO_2H_{1.6}$ exhibits a hydride conductivity of 2.1×10^{-4} S/cm at 300° C with an activation energy of 68.4 kJ/mol.

In order to further verify the occurrence of H^- ion conduction, Kobayashai *et.al*. constructed an all-solid-state cell with configuration Ti/*o*-La_2LiHO_3/TiH_2 which demonstrated the battery reaction as a consequence of hydride ion diffusion.[10]

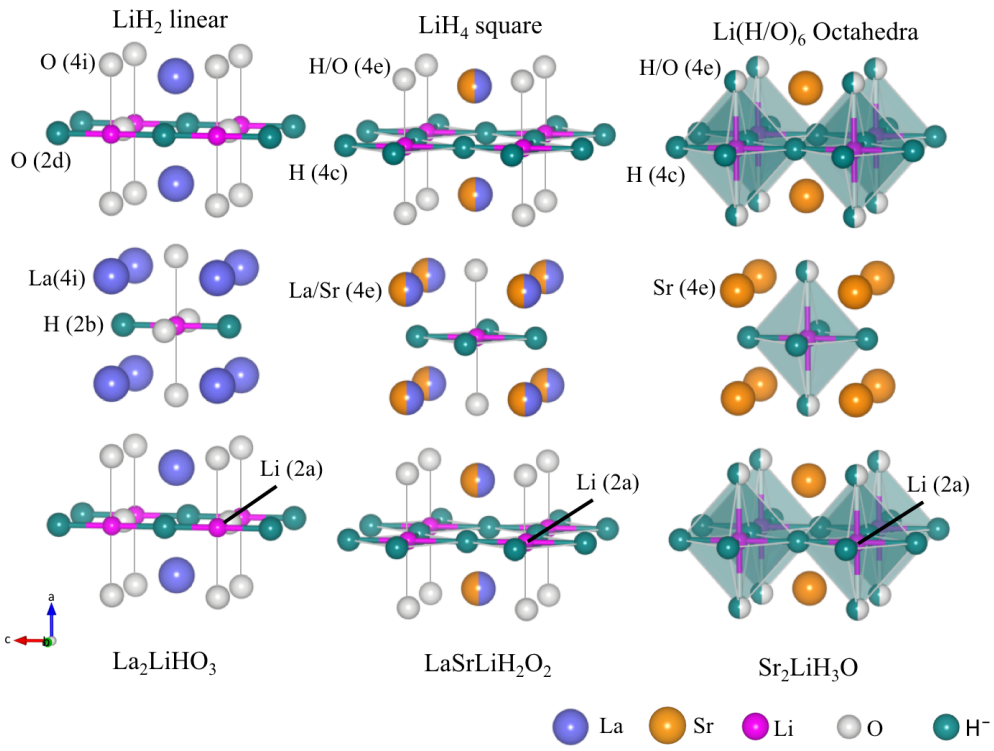

Figure 1.4 Crystal structures of LSLHO family of oxyhydrides showing the increasing carrier concentration by aliovalent substitution

Iwasaki *et.al.* investigated the rare earth substitution in oxyhydrides Ln_2LiHO_3 (Ln = La, Pr, Nd) to see the effect over crystal structure, ionic conductivity and thermal stability. The comparison of the ionic conductivities at 280° C showed a gradual increase with decreasing lanthanide ionic size. Phase identification revealed that *Ln* = La, Pr and Nd systems possessed isostructural phases and the anion distribution varied depending upon the *Ln* element. The hydride ion diffusion is facilitated by axial site disorder and low oxide ion content resulting in highest conductivity of 2.2×10^{-5} S/cm for Nd_2LiHO_3. [59]

1.7 Aim of study

The hydride ion in LSLHO family of oxyhydrides mainy conducted through the perovskite layer owing to its preferential occupation at the equatorial sites as verified by theoretical calculations. [60] Controlling site selectivity to tailor the anionic sublattices to have preferred anionic arrangement is a bigger challenge in solid state ionics. In isostructural oxides $Ln_2NiO_{4+\delta}$, fast O^{2-} conduction via apical sites has been previously reported.[55,56] In the present work we aim to study the site selectivity of H^- ions as a consequence of changing B site cations. For this purpose, we plan to use high valent larger B site cations (i.e. Sc^{3+} and Y^{3+})

compared to Li^+ which was employed in LSLHO oxyhydrides. The anticipated change of anionic arrangement may provide us an opportunity to study another H^- diffusion pathway for fast H^- diffusion. Apart from site selectivity, a large B site cation may help to enlarge the bottleneck for fast ionic diffusion. Chapter 3 reports a successful synthesis of a new H^- conductive oxyhydride Ba_2ScHO_3 with K_2NiF_4-type structure where H^- anions selectively occupy the apical site in contrast to the reported Li-based series. In chapter 4 we have described the high-pressure synthesis of a yttrium-based oxyhydride Ba_2YHO_3, which adopts a structure with "complete" H^-/O^{2-} anion ordering to form $[Ba_2H_2]$ rock-salt layers.

References

[1] Yamamoto, O. Solid state ionics: A Japan perspective. *Sci. Technol. Adv. Mat.* **2017**, 18, 504–527.

[2] Kawamura, J. Ion conducting materials: Superionic conductors and solid-state ionics. In *Reference Module in Materials Science and Materials Engineering*; Elsevier, 2017.

[3] Azad, A. M.; Akbar, S. A.; Mhaisalkar, S. G.; Birkefeld, L. D.; Goto, K. S. Solid-state gas sensors: A review. *J. Electrochem. Soc.* **1992**, *139*, 3690.

[4] Mahato, N.; Banerjee, A.; Gupta, A.; Omar, S.; Balani, K. Progress in material selection for solid oxide fuel cell technology: A Review. *Prog. Mat. Sci.* **2015**, *72*, 141–337.

[5] Ohno, S.; Banik, A.; Dewald, G. F.; Kraft, M. A.; Krauskopf, T.; Minafra, N.; Till, P.; Weiss, M.; Zeier, W. G. Materials Design of Ionic Conductors for Solid State Batteries. *Prog. Energy.* **2020**, 2 022001.

[6] West, A. R. *Solid State Chemistry and Its Applications*; John Wiley & Sons, 2014.

[7] Tuller, H. Ionic Conduction and Applications. In *Springer Handbook of Electronic and Photonic Materials*; Kasap, S., Capper, P., Eds.; Springer International Publishing: Cham, 2017.

[8] West, A. R. Solid Electrolytes. *Berichte der Bunsengesellschaft für physikalische Chemie* **1989**, 93, 1235–1241.

[9] Verbraeken, M. C.; Cheung, C.; Suard, E.; Irvine, J. T. S. High H− ionic conductivity in barium hydride. *Nat. Mat.* **2015**, 14, 95–100.

[10] Kobayashi, G.; Hinuma, Y.; Matsuoka, S.; Watanabe, A.; Iqbal, M.; Hirayama, M.; Yonemura, M.; Kamiyama, T.; Tanaka, I.; Kanno, R. Pure H^- conduction in oxyhydrides. *Science* **2016**, 351, 1314–1317.

[11] Nakamura, O.; Kodama, T.; Ogino, I.; Miyake, Y. High-conductivity solid proton conductors: Dodecamolybdophosphoric acid and dodecatungstophosphoric acid crystals. *Chem. Lett.* **1979**, 8, 17–18.

[12] Baranov, A. I.; Shuvalov, L. A.; Shchagina, N. M. Superionic conductivity and phase transitions in $CsHSO_4$ and $CsHSeO_4$ crystals. *JETP Lett.* **1982** 36*, 459-462.*

[13] Wu, J.; Li, L. P.; Espinosa, W. T. P.; Haile, S. M. Defect chemistry and transport properties of $Ba_xCe_{0.85}M_{0.15}O_{3-\delta}$. *J. Mat. Res.* **2004**, 19, 2366–2376.

[14] Kamaya, N.; Homma, K.; Yamakawa, Y.; Hirayama, M.; Kanno, R.; Yonemura, M.; Kamiyama, T.; Kato, Y.; Hama, S.; Kawamoto, K.; Mitsui, A. A lithium superionic conductor. *Nat. Mat.* **2011**, 10, 682–686.

[15] Inaguma, Y.; Liquan, C.; Itoh, M.; Nakamura, T.; Uchida, T.; Ikuta, H.; Wakihara, M. High Ionic Conductivity in Lithium Lanthanum Titanate. *Solid. Stat. Commun.* **1993**, 86, 689–693.

[16] Hong, H. Y. P. Crystal structure and ionic conductivity of $Li_{14}Zn(GeO_4)_4$ and other new Li^+ superionic conductors. *Mat. Res. Bull.* **1978**, 13, 117–124.

[17] Harada, Y.; Hirakoso, Y.; Kawai, H.; Kuwano, J. Order–disorder of the A-site ions and lithium ion conductivity in the Perovskite solid solution $La_{0.67-x}Li_{3x}TiO_3$ (X = 0.11). *Solid State Ionics* **1999**, 121, 245–251.

[18] Takahashi, T. Recent trends in high conductivity solid electrolytes and their applications: an overview. In *Superionic solids and solid electrolytes recent trends*; Laskar, A. L., Chandra, S., Eds.; Academic Press, 1989; pp 1–41.

[19] Goodenough, J. B.; Hong, H. Y.-P.; Kafalas, J. A. Fast Na+ ion transport in skeleton structures. *Mat. Res. Bull.* **1976**, 11, 203–220.

[20] Nomura, K.; Ikeda, S.; Ito, K.; Einaga, H. Framework structure, phase transition, and transport properties in $M^{II}Zr_4(PO_4)_6$ Compounds (M^{II} = Mg, Ca, Sr, Ba, Mn, Co, Ni, Zn, Cd, and Pb). *BCSJ* **1992**, 65, 3221–3227.

[21] Matsui, T.; Wagner, J. B. Inorganic copper ion conductors. In *Solid Electrolytes*; Hagenmuller, P., Van gool, W., Eds.; Academic Press, 1978; pp 237–252.

[22] Geller, S.; Akridge, J. R.; Wilber, S. A. Crystal Structure and Conductivity of the Solid Electrolyte α-$RbCu_4C1_3I_2$. *Phys. Rev. B* **1979**, 19, 5396–5402.

[23] Turković, A.; Gržeta-Plenković, B.; Etlinger, B. Stability of the α-$RbCu_4C_{l3}I_2$ solid-electrolyte cell. *Il Nuovo Cimento D* **1983**, 2, 1977–1981.

[24] Kasper, J. S. 14 - Inorganic Silver Ion Conductors. In *Solid Electrolytes*; Hagenmuller, P., Van gool, W., Eds.; Academic Press, 1978; pp 217–235.

[25] Šušić, M. V.; Mentus, S. V. Electrochemical behaviour of the solid electrolyte Ag6I4WO4. *Electrochimica Acta* **1983**, 28, 35–41.

[26] Dell, R. M.; Hooper, A. 18 - Oxygen Ion Conductors. In *Solid Electrolytes*; Hagenmuller, P., Van gool, W., Eds.; Academic Press, 1978; pp 291–312.

[27] Duran, P.; Jurado, J. R.; Moure, C.; Valverde, N.; Steele, B. C. H. High oxygen ion conduction in some Bi_2O_3-Y_2O_3 (Er_2O_3) solid solutions. *Mat. Chem. Phy.* **1987**, 18, 287–294.

[28] Ishihara, T.; Shibayama, T.; Honda, M.; Nishiguchi, H.; Takita, Y. Intermediate temperature solid oxide fuel cells using $LaGaO_3$ electrolyte II. Improvement of oxide ion conductivity and power density by doping Fe for Ga site of $LaGaO_3$. *J. Electrochem. Soc.* **2000**, 147, 1332-1337.

[29] Kanno, R.; Nakamura, S.; Ohno, K.; Kawamoto, Y. Ionic Conductivity of Tetragonal $PbSnF_4$ Prepared by Solid State Reaction in HF Atmosphere. *Mat. Res. Bull.* **1991**, 26 (11), 1111–1117.

[30] Réau, J. M.; Portier, J. Fluorine ion conductors. In *Solid Electrolytes*; Hagenmuller, P., Van gool, W., Eds.; Academic Press, 1978; pp 313–333.

[31] Berastegui, P.; Hull, S. Structure and conductivity of some fluoride ion conductors. *Solid State Ionics* **2002**, 154–155, 605–608.

[32] Bloom, H.; Heymann, E. The Electric Conductivity and the activation energy of ionic migration of molten salts and their mixtures. *Proceedings of the Royal Society of London. Series A, Mathematical and Physical Sciences* **1947**, 188, 392–414.

[33] Murin, I. V.; Glumov, O. V.; Mel'nikova, N. A. Solid electrolytes with predominant chloride conductivity. *Russ. J. Electrochem.* **2009**, 45, 411–416.

[34] Fukui, K.; Iimura, S.; Tada, T.; Fujitsu, S.; Sasase, M.; Tamatsukuri, H.; Honda, T.; Ikeda, K.; Otomo, T.; Hosono, H. Characteristic fast H^- ion conduction in oxygen-substituted lanthanum hydride. *Nat. Commun.* **2019**, 10, 2578.

[35] Andresen, A. F.; Maeland, A. J.; Slotfeldt-Ellingsen, D. Calcium hydride and deuteride studied by neutron diffraction and NMR. *J. Sol. Stat. Chem.* **1977**, 20, 93–101.

[36] Verbraeken, M. C.; Suard, E.; Irvine, J. T. S. Structural and electrical properties of calcium and strontium hydrides. *J. Mat. Chem.* **2009**, 19, 2766.

[37] Kanno, R.; Kobayashi, G.; Suzuki, K.; Hirayama, M.; Mori, D.; Tamura, K. Synthesis and Structures of novel solid-state electrolytes. In *Nanoinformatics*; Tanaka, I., Ed.; Springer Singapore: Singapore, 2018; pp 279–298.

[38] Hayashi, K.; Matsuishi, S.; Kamiya, T.; Hirano, M.; Hosono, H. Light-induced conversion of an insulating refractory oxide into a persistent electronic conductor. *Nature* **2002**, 419, 462–465.

[39] Hayashi, K.; Hirano, M.; Matsuishi, S.; Hosono, H. Microporous crystal $12CaO{\cdot}7Al_2O_3$ encaging abundant o- radicals. *J. Am. Chem. Soc.* **2002**, 124, 738–739.

[40] Kobayashi, Y.; Hernandez, O. J.; Sakaguchi, T.; Yajima, T.; Roisnel, T.; Tsujimoto, Y.; Morita, M.; Noda, Y.; Mogami, Y.; Kitada, A.; Ohkura, M.; Hosokawa, S.; Li, Z.;

Hayashi, K.; Kusano, Y.; Kim, J. eun; Tsuji, N.; Fujiwara, A.; Matsushita, Y.; Yoshimura, K.; Takegoshi, K.; Inoue, M.; Takano, M.; Kageyama, H. An oxyhydride of batio3 exhibiting hydride exchange and electronic conductivity. *Nat. Mat.* **2012**, 11, 507–511.

[41] Sakaguchi, T.; Kobayashi, Y.; Yajima, T.; Ohkura, M.; Tassel, C.; Takeiri, F.; Mitsuoka, S.; Ohkubo, H.; Yamamoto, T.; Kim, J. eun; Tsuji, N.; Fujihara, A.; Matsushita, Y.; Hester, J.; Avdeev, M.; Ohoyama, K.; Kageyama, H. Oxyhydrides of (Ca,Sr,Ba)TiO_3 perovskite solutions. *Inorg. Chem.* **2012**, 51, 11371–11376.

[42] Ubukata, H.; Broux, T.; Takeiri, F.; Shitara, K.; Yamashita, H.; Kuwabara, A.; Kobayashi, G.; Kageyama, H. Hydride Conductivity in an Anion-Ordered Fluorite Structure LnHO with an Enlarged Bottleneck. *Chem. Mater.* **2019**. 31, 7360-7366.

[43] Yamashita, H.; Broux, T.; Kobayashi, Y.; Takeiri, F.; Ubukata, H.; Zhu, T.; Hayward, M. A.; Fujii, K.; Yashima, M.; Shitara, K.; Kuwabara, A.; Murakami, T.; Kageyama, H. Chemical pressure-induced anion order–disorder transition in lnho enabled by hydride size flexibility. *J. Am. Chem. Soc.* **2018**, 140, 11170–11173.

[44] Bridges, C. A.; Darling, G. R.; Hayward, M. A.; Rosseinsky, M. J. Electronic structure, magnetic ordering, and formation pathway of the transition metal oxide hydride $LaSrCoO_3H_{0.7}$. *J. Am. Chem. Soc.* **2005**, 127, 5996–6011.

[45] Hayward, M. A.; Cussen, E. J.; Claridge, J. B.; Bieringer, M.; Rosseinsky, M. J.; Kiely, C. J.; Blundell, S. J.; Marshall, I. M.; Pratt, F. L. The hydride anion in an extended transition metal oxide array: $LaSrCoO_3H_{0.7}$. *Science* **2002**, 295, 1882–1884.

[46] Helps, R. M.; Rees, N. H.; Hayward, M. A. An extended transition metal oxide-hydride. *Inorg. Chem.* **2010**, 49, 11062–11068.

[47] Tassel, C.; Goto, Y.; Watabe, D.; Tang, Y.; Lu, H.; Kuno, Y.; Takeiri, F.; Yamamoto, T.; Brown, C. M.; Hester, J.; Kobayashi, Y.; Kageyama, H. High-pressure synthesis of manganese oxyhydride with partial anion order. *Angew. Chem.* **2016**, 128, 9819–9822.

[48] Kobayashi, Y.; Hernandez, O.; Tassel, C.; Kageyama, H. New chemistry of transition metal oxyhydrides. *Sci. Technol. Adv. Mat.* **2017**, 18, 905–918.

[49] Masuda, N.; Kobayashi, Y.; Hernandez, O.; Bataille, T.; Paofai, S.; Suzuki, H.; Ritter, C.; Ichijo, N.; Noda, Y.; Takegoshi, K.; Tassel, C.; Yamamoto, T.; Kageyama, H. Hydride in $BaTiO_{2.5}H_{0.5}$: A labile ligand in solid state chemistry. *J. Am. Chem. Soc.* **2015**, 137, 15315–15321.

[50] Yamamoto, T.; Zeng, D.; Kawakami, T.; Arcisauskaite, V.; Yata, K.; Patino, M. A.; Izumo, N.; McGrady, J. E.; Kageyama, H.; Hayward, M. A. The role of π-blocking

hydride ligands in a pressure-induced insulator-to-metal phase transition in $SrVO_2H$. *Nature Commun.* **2017**, 8, 1217

[51] Tang, Y. Studies on perovskite oxyhydrides: catalysis and hydride anion diffusion. Dissertation. 2018. doi.org/14989/doctor.k21271

[52] Tilley, R. J. D. *Perovskites-structure-property-relationship*s; Wiley, 2016.

[53] Goldschmidt, V. M. Die Gesetze der Krystallochemie. *Naturwissenschaften* **1926**, 14, 477–485.

[54] Liu, X.; Hong, R.; Tian, C. Tolerance factor and the stability discussion of abo_3-type ilmenite. *J Mater Sci: Mater. Electron.* **2009**, 20, 323–327.

[55] Skinner, S. J. Characterisation of $La_2NiO_{4+\delta}$ using in-situ high temperature neutron powder diffraction. *Solid State Sciences* **2003**, 5, 419–426.

[56] Lee, D.; Lee, H. N. Controlling oxygen mobility in ruddlesden–popper oxides. *Materials (Basel)* **2017**, 10. 368.

[57] Fuertes, A. Prediction of anion distributions using pauling's second rule. *Inorganic Chemistry* **2006**, *45* (24), 9640–9642.

[58] Kobayashi, Y.; Tsujimoto, Y.; Kageyama, H. Property engineering in perovskites via modification of anion chemistry. *Annual Review of Materials Research* **2018**, *48* (1), 303–326.

[59] Iwasaki, Y.; Matsui, N.; Suzuki, K.; Hinuma, Y.; Yonemura, M.; Kobayashi, G.; Hirayama, M.; Tanaka, I.; Kanno, R. Synthesis, crystal structure, and ionic conductivity of hydride ion-conducting Ln_2LiHO_3 (Ln = La, Pr, Nd) oxyhydrides *J. Mat. Chem. A* **2018**, 6, 23457–23463.

[60] Fjellvåg, Ø. S.; Armstrong, J.; Sławiński, W. A.; Sjåstad, A. O. Thermal and structural aspects of the hydride-conducting oxyhydride La_2LiHO_3 obtained via a halide flux Method. *Inorg. Chem.* **2017**, 56, 11123–11128.

Chapter 2

Experimental

2.1 Material preparation: high pressure synthesis

The inclusion of pressure variable in solid state synthesis significantly expands the range of compositions that can be made. The densification of solids derived by high pressure leads to unusual metastable compounds which often accompanies dramatic changes in physical properties such as magnetism, electrical conductivity, optical absorption and resistance to shear. These unusual and interesting properties are retained upon decompression which make the high pressure technique suitable to obtain metastable phases.[1]

Figure 2(a) shows the high-pressure apparatus used for the synthesis. It consists of six anvils, four of which surround the cell horizontally and the remaining two are the bottom and the top one. The pressure is transferred from all six sides isotropically. The effective pressure was calibrated by measuring the change in resistivity of Bismuth as a result of changing pressure.[2] The cell assembly used for the high pressure consisted of 16mm pyrophyllite cube drilled through center. One end of the pyrophyllite cube is closed by a pyrophyllite pallet. A Mo film to ensure connection and NaCl pallet to avoid mixing were placed successively. A graphite heater sleeve was then placed in a drilled pyrophyllite block which contained inner NaCl and BN sleeves (Figure 2.1b). The samples were loaded in the cell in an Ar-filled glove box and other end was sealed similar to the base. A computer program allowed the control of voltage and current which helped to manipulate the heating cycle for sintering.

In the present study the ball milled analytical grade precursors were formed into pallet shape in an Argon filled glove box and were sintered at 2-4 GPa pressure and temperature ranging from 550-1000°C depending upon the composition.

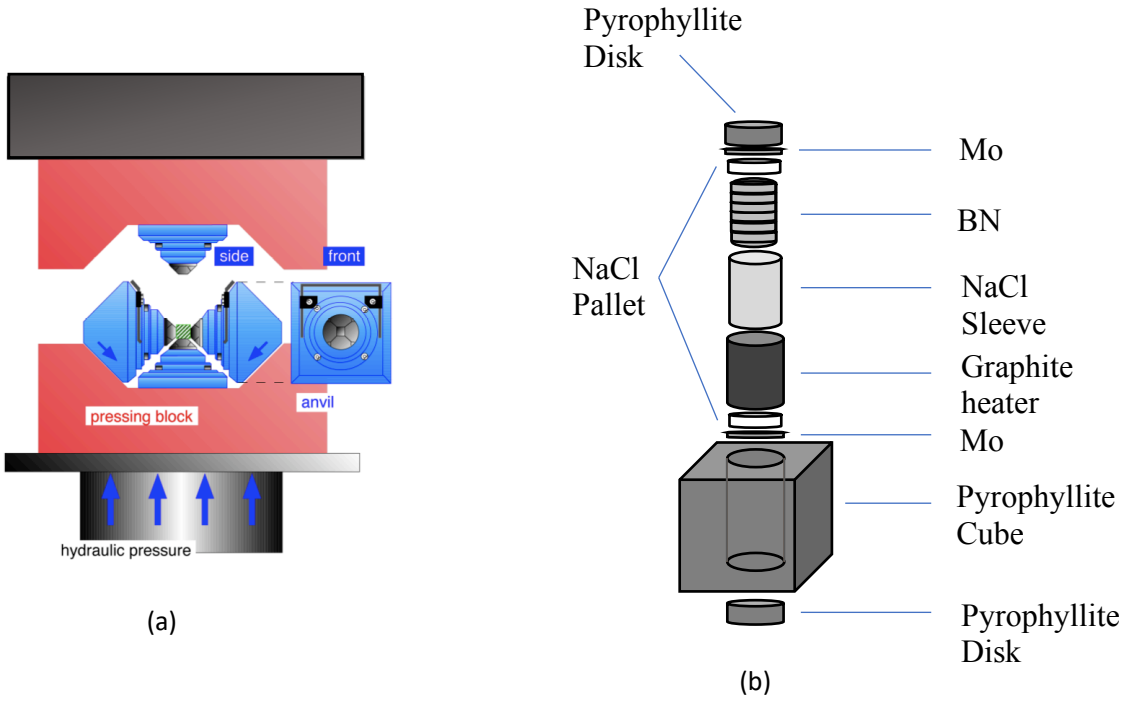

Figure 2.1 (a) Cubic Anvil apparatus and (b) assembly of pyrophyllite cube for high pressure synthesis

2.2.1 X-ray diffraction

X-ray diffraction (XRD) is a rapid characterization technique which provides information about phase and unit cell dimensions for bulk composition. The interaction of monochromatic radiations produces constructive interference when condition of Bragg's law (eqn 2.1) is satisfied. The law gives a relationship between wavelength of incident radiation to diffraction angle and lattice spacing in a crystalline sample.

$$n\lambda = 2dSin\theta \qquad (2.1)$$

The random orientation of the polycrystalline samples allows the scanning of all possible diffraction directions of the lattice by scanning the sample through a range of 2θ angles.[3] For all the oxyhydride samples, X-ray diffractometer (Miniflex600, Rigaku) with Cu Kα was used. The sample were scanned in the range from 10° - 80° at each 0.02° step. Since the oxyhydrides are highly air and moisture sensitive, therefore the samples were loaded into aluminum sample holder covered with a kapton film in an Ar-filled glove box. Reitan FP program was used to refine the lattice and structural parameters.

2.2.2 Synchrotron X-ray diffraction

Synchrotron X-ray diffraction (SXRD) data for oxyhydrides was obtained at room temperature using a high-resolution angle-dispersive type X-ray diffractometer (BL02B2 and BL19B2) installed at the SPring-8. The specimens were sealed in a glass capillary (ca. 0.3 mmϕ) which was filled by Ar for room temperature X-ray diffraction measurements. Diffraction data for Ba_2ScHO_3 samples were collected with a 0.01° step width from 3.0° to 78.0° in 2θ, whereas for Ba_2YHO_3 samples, the data was collected from 2.1° to 78.2° in 2θ with a 0.006° step width. In order to avoid the preferential orientation of crystallites, the sealed capillary was rotated during the measurement. The wavelengths of the incident beams were calibrated with NIST SRM Ceria 640b CeO_2 fixed at 0.5 Å and 0.8 Å for Ba_2ScHO_3 and Ba_2YHO_3 samples respectively.

2.2.3 Neutron diffraction

While X-rays interacts primarily with electron cloud surrounding the atom, neutron scattering occurs because of interaction of neutrons with nucleus. For this reason, neutron scattering occurs equally for heavier as well as lighter elements. Because of these different scattering properties, certain complementary information can be obtained which is not accessible by X-ray diffraction. In particular, for hydrogen in crystal lattice of metals, neutron diffraction is the only technique locating hydrogen atoms in the structure. Thus, for metal hydrides and oxyhydrides, neutron diffraction is primary choice to detect the hydrogen precisely.[4]

Room temperature neutron powder diffraction (NPD) measurements for oxyhydride samples was carried out by time-of-flight (TOF) neutron SPICA powder diffractometer installed at J-PARC. Sample was placed in cylindrical vanadium cell (6mm radius, 55mm height) and diffraction data was collected at room temperature. Z-Rietveld program was used to refine lattice and structural parameters.[5] Vesta software was used to the illustrate crystal structures.[6]

2.2.4 Reitveld analysis

A refinement technique was developed by Hugo Reitveld in 1960s to characterize the crystalline materials. The X-ray and Neutron diffraction patterns of powder sample contains reflections at certain positions. Many structural aspects of materials are in fact determined by the height, width and peak position of these reflections. The Reitveld method is used to fit the

calculated profile (structural and instrumental parameters) to experimental data. In order to carry out the refinement using non-linear least squares method, a reasonable approximation is made for many free parameters which include peak shape, unit cell dimensions and coordinates of the all the corresponding atoms in the structure.

In Rietveld analysis the sum of weighted squares of residuals is minimized by refining x ($x_1, x_2, x_3, \cdots x_n$) successively (x represents the powder diffraction patterns). The refinement proceeds by fitting the calculated powder pattern to the observed one by a nonlinear least-squares method.

$$S(x) = \sum_{i=0}^{n} wi[y_i - f_i(x)]^2 \qquad (2.2)$$

In equation 2.2, i is the step number, N represents total number of data points, w_i is the statistical weight based on counting statistics, y_i is the observed intensity and $f_i(x) \equiv f(2\theta; x_1, x_2, x_3 \ldots x_n)$ is the calculated intensity at diffraction angle of $2\theta_i$.

In angle-dispersive powder diffraction, the observed intensity, y_i, at a particular step, i, is modeled by the calculated intensity, $f_i(x)$, which is the sum of contributions from Bragg reflections plus background correction $y_b(2\theta_i)$:

$$fi(x) = S_R(\theta_i)A(\theta_i)D(\theta_i)s \sum_K m_K |F(\boldsymbol{h}_K)|^2 P_K L(\theta_K)\, G(\Delta 2\theta_{iK}) + y_b(2\theta_i) \qquad (2.3)$$

where

$S_R(\theta_i)$ = correction factor for surface roughness

$A(\theta_i)$ = absorption factor (transmission coefficient)

$D(\theta_i)$ = correction factor for the constant irradiation width

s = scale factor for the particular phase

K = reflection number

m_K = multiplicity

$F(\boldsymbol{h}_K)$ = structure factor

$\boldsymbol{h}_K$ = reflection indices hkl

P_K = correction factor for preferred orientation

$L(\theta_K)$ = Lorentz and polarization factors (the polarization factor is unnecessary in neutron diffraction)

θ_K = Bragg angle

$G(\Delta 2\theta_{iK}) \equiv G(2\theta_i - 2\theta_K)$ = profile function.

Equation 2.3 is formulated for pure samples, in case of samples with multiple phases, different scale factors needs to be assigned to all the crystalline phases present. Accordingly, the 1st term on the right side of equation 2.3 is summed up for all the phases (j 1, 2, …) and the equation becomes

$$fi(x) = S_R(\theta_i)A(\theta_i)D(\theta_i)s\sum_K m_{iK}\left|F_j(\boldsymbol{h}_K)\right|^2 P_{jK}L(\theta_K)\,G_j(\Delta 2\theta_{iK}) + y_b(2\theta_i) \qquad (2.4)$$

The successive refinements are carried out so that $f_i(x)$ approaches the observed intensity. Following are groups of least squares parameters which are generally refined in a Reitveld refinement.

- Background parameters
- Peak shift parameters
- Multiple peak shape parameters (FWHM and asymmetry)
- Unit cell dimensions (a, b, c α, β, γ), depending on the crystal family/system, for different phase present

- Preferred orientation, and sometimes absorption, porosity, and extinction coefficients, which can be independent for different phases present.
- Scale factors (for each phase)
- Atomic positions
- Occupancy at atoms at different sites
- Atomic displacement parameters
    - Isotropic and anisotropic (temperature) parameters.

The quality of Reitveld refinement is determined by numerical figure of merit. Following reliability indices characterize the quality of the refinement.

$$R_{wp} = \left\{ \frac{\sum_{i=0}^{N} \omega_i [y_i - f_i(x)]^2}{\sum_{i=0}^{N} \omega_i y_i^2} \right\}^{1/2} \tag{2.5}$$

R_{wp} (R-weighed pattern) is the most significant of the reliability indices as the quantity in the numerator is actually minimized in the least square refinement.

R_p (R-pattern) is defined as

$$R_p = \frac{\sum_{i=0}^{N} |y_i - f_i(x)|}{\sum_{i=0}^{N} y_i} \tag{2.6}$$

A variation of R_p is R_R (R-Reitveld) which is defined as

$$R_R = \frac{\sum_{i=0}^{N} |y_i - f_i(x)|}{\sum_{i=0}^{N} |y_i - y_b(2\theta_i|} \tag{2.7}$$

R_e (R-expected) is derived from the statistical error associated with the measured intensities:

$$R_e = \left[(N-n) / \sum_{i=0}^{N} \omega_i y_i^2 \right]^{1/2} \tag{2.8}$$

The goodness-of-fit indicator S is given by

$$S = \frac{R_{wp}}{R_e} = \left\{ \frac{\sum_{i=0}^{N} \omega_i [y_i - f_i(x)]^2}{(N-n)} \right\}^{1/2} \tag{2.9}$$

R_B (R-Bragg factor) and R_f (R-structure factor) are as defined as

$$R_B = \frac{\sum_K |I_o(\boldsymbol{h}_K) - I(\boldsymbol{h}_K)|}{\sum_K I_o(\boldsymbol{h}_K)} \tag{2.10}$$

$$R_B = \frac{\sum_K |F_o(\boldsymbol{h}_K) - F(\boldsymbol{h}_K)|}{\sum_K F_o(\boldsymbol{h}_K)} \tag{2.11}$$

R_{wp} and R_p are more useful in determining the progress of a particular Reitveld refinement. The refinement carried out with different data sets and even by different materials cannot be compared in terms of these two reliability indices as these are influenced mostly by the intensity of the diffraction line and the background level. A quality of fit is rather best judged by ratio of the final R_{wp} to the expected R_{wp} (R_e) which is called S, the goodness of fit indicator. It can have minimum value of unity which is virtually possible when the refinement is complete. However, S ≤1.3 is considered quite satisfactory.

Apart from the reliability indices which describe the agreement between observed and calculated diffraction patterns and backgrounds, the reliability of the fitting still depends on several other factors such as a data quality, reasonable structural model, negligible effects of preferred orientation and coarse particles and user expertise.[7,8]

2.2.5 Bond valence sum

Bond valence sum is an important tool to know about the plausibility of inorganic crystal structures. The model is constructed on Pauling's electrostatic valence concept. According to which the valence V_{ij} of a bond between two atoms i and j is defined in a way that sum of all the valences from a given atom i with valence V_{ij} obey:

$$Vi = \sum_j V_{ij} \tag{2.12}$$

The variation of bond length with valence is depicted by the following empirical relationship

$$V_{ij} = \exp\left[(R_{ij} - d_{ij})/b\right] \tag{2.13}$$

B is a universal constant with a value of 0.37Å. From these two equations the value of R_{ij} is calculated which is rereferred as bond valence parameter. [ref]

The agreement between oxidation states (formal ionic charges) and bond valence sum

calculated by the above method helps to check and validate new crystal structures. For correct structures the agreement is generally good, otherwise in case of large deviations the structure determination is prone to errors (incorrect symmetry or missing atoms).[9,10]

2.3 Electrochemical impedance spectroscopy (EIS)

The measure of the opposition to electrical current in a circuit when voltage is applied, is defined as electrical impedance. Impedance is considered simply a resistance when it is frequency independent as given by Ohm's law

$$R = \frac{V}{I} \tag{2.14}$$

Where V is the voltage, I is the current in amperes and R is the resistance in Ohms. Instead of resistance, impedance is more general circuit parameter which is frequency dependent. In electrochemical impedance spectroscopy, both V and I are time independent sinusoidal functions.

$$V(t) = V_o Sin(\omega t) \tag{2.15}$$

Where V_o is the amplitude and ω is the radial frequency. The radial frequency is converted to linear frequency as $\omega = 2\pi f$. The current has a phase shift φ and an amplitude I_o

$$I(t) = I_o Sin(\omega t + \varphi) \tag{2.16}$$

The impedance can be calculated by an expression similar to Ohm's law as

$$Z = \frac{V(t)}{I(t)} = \frac{V_o Sin(\omega t)}{I_o Sin(\omega t + \varphi)} = Z_o \frac{Sin(\omega t)}{Sin(\omega t + \varphi)} \tag{2.17}$$

Here Z_o is the magnitude and φ is phase shift.
In terms of Euler's relationship

$$e^{j\varphi} = cos\varphi + jsin\varphi \text{c} \tag{2.18}$$

Since impedance is a complex function, both potential and current can be expressed as

$$V(t) = V_o e^{(j\omega t)} \tag{2.19}$$

$$I(t) = I_o e^{(j\omega t - \varphi)} \tag{2.20}$$

Impedance in the form of complex number is represented as

$$Z_{(\omega)} = \frac{V}{I} = Z_o e^{(j\varphi)} = Z_o(cos\varphi + jsin\varphi) \tag{2.21}$$

Above equation shows $Z_{(\omega)}$ is composed of a real and an imaginary component. Plotting the real part on X-axis and imaginary part on Y-axis gives a Nyquist Plot.

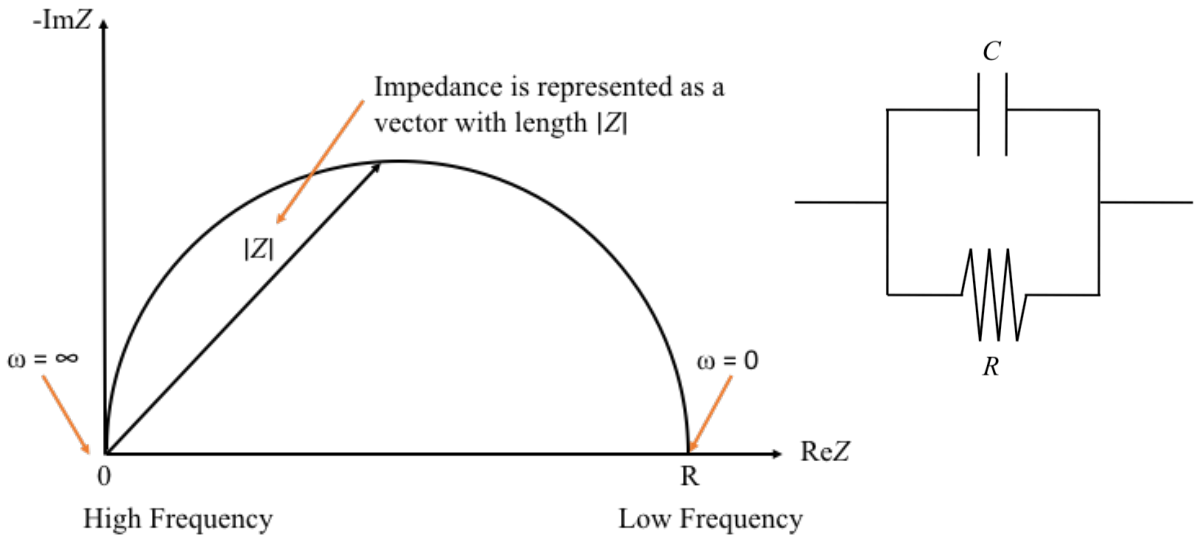

Figure 2.2 Nyquist plot(left) resulted from an equivalent electrical circuit(right)

The data obtained from EIS is commonly analyzed by fitting to an equivalent circuit. The circuit elements in the model are common electrical elements such a resistor, inductor and capacitor which should have basis in the physical electrochemistry of the system under study. Impedance of the resistor as mentioned earlier is frequency independent, whereas that of inductor increases with frequency and capacitor has opposite behavior to an inductor.

In order to measure the impedance of the sample by EIS, the sample is scanned in a wide range of frequency, typically 10^{-2} – 10^{7}Hz. Different regions of the ceramic sample behave as resistor and capacitor, usually placed in parallel. From the impedance spectrum, different

RC components can be identified which are separated by frequency domain. A typical spectrum of an electroceramic sample shows distinct features which can be attributed to intragrain or bulk and intergrain or grain boundary regions. Ideally each parallel RC element gives rise to corresponding semicircles from which R and C values can be extracted. The assignment of R and C values to different regions of the sample depends on the magnitude of the capacitances.[11]

References

(1) McMillan, P. F. High pressure synthesis of solids. *Current Opinion in Solid State and Mat. Sci.* **1999**, 4, 171–178.

(2) Ito, E. Pressure calibration for multi-anvil apparatuses in high-pressure earth science. *The Review of High Pressure Science and Technology* **2003**, 13, 265–269.

(3) Cullity, B. D.; Stock, S. R. *Elements of X-Ray Diffraction*, 2nd ed.; Addison-Wesley Publishing Company INC, California, U.S, 1978.

(4) Fritzsche, H., Huot, J., Fruchart, D., *Neutron Scattering and Other Nuclear Techniques for Hydrogen in Materials*, Springer International Publishing, 2016.

(5) Oishi, R.; Yonemura, M.; Nishimaki, Y.; Torii, S.; Hoshikawa, A.; Ishigaki, T.; Morishima, T.; Mori, K.; Kamiyama, T. Rietveld analysis software for J-PARC. *Nuclear Instruments and Methods in Physics Research Section A: Accelerators, Spectrometers, Detectors and Associated Equipment* **2009**, 600*,* 94–96.

(6) Momma, K. VESTA 3 for Three-dimensional visualization of crystal, volumetric and morphology data. *J. Appl. Crystallogr.* **2011**, 44, 1272–1276.

(7) Izumi, F.; Momma, K. Three-dimensional visualization in powder diffraction. *Solid State Phenomena* **2007,** 130, 15-20.

(8) Toby, B. H. R Factors in Rietveld Analysis: How Good Is Good Enough? *Powder Diffraction* **2006**, 21, 67–70.

(9) Brese, N. E.; O'Keeffe, M. Bond-valence parameters for solids. *Acta. Cryst. Sec. B* **1991**, 47, 192–197.

(10) Brown, I. D.; Altermatt, D. Bond-valence parameters obtained from a systematic analysis of the Inorganic crystal structure database. *Acta Cryst. Sec. B* **1985**, 41, 244–247.

(11) Irvine, J. T. S.; Sinclair, D. C.; West, A. R. Electroceramics: Characterization by impedance spectroscopy. *Adv. Mat.* **1990**, 2, 132–138.

Chapter 3

Ba_2ScHO_3: H^- Conductive Layered Oxyhydride with H^- Site Selectivity

Abstract:

Hydride (H^-) conduction is a new frontier related to hydrogen transport in solids. Here, a new H^- conductive oxyhydride Ba_2ScHO_3 was successfully synthesized using a high-pressure technique. Powder X-ray and neutron diffraction experiments investigated the fact that Ba_2ScHO_3 adopts a K_2NiF_4-type structure with H^- ions preferentially occupying the apical sites, as supported by theoretical calculations. Electrochemical impedance spectra showed that Ba_2ScHO_3 exhibited H^- conduction and a conductivity of 5.2×10^{-6} S cm^{-1} at 300 ºC. This value is much higher than that of $BaScO_2H$, which has an ideal perovskite structure, suggesting the advantage of layered structures for H^- conduction. Tuning site selectivity of H^- ions in layered oxyhydrides might be a promising strategy for designing fast H^- conductors applicable for novel electrochemical devices.

3.1 Introduction

A hydride ion (H^-) is an attractive charge carrier because it exhibits promising features for fast ionic conduction; namely, monovalence, suitable ionic size similar to that of F^- and O^{2-}, and high polarizability. Hydride ion conduction in solids was first pointed out in 1977 by detecting the dynamics of hydrogen in CaH_2 using ^{1}H NMR spectroscopy[1]. Subsequently, H^- conductivities of Ba_2NH[2, 3] and $AE_{1-x}Na_xH_{2-x}$ (AE = Ca, Sr)[4] were reported, and recently, evidence of a H^- conduction phenomenon was confirmed by electromotive force measurements in BaH_2.[5] However, metal hydrides without electron (or hole) conduction are almost limited to alkali- and alkali earth ones owing to the strong reducing property of H^-, permitting only simple compositions and structures such as AH and AEH_2 (A = alkali, AE = alkali earth). This constraint prevents designing H^- concentrations and diffusion pathways, and thus requires alternative approaches for further development of H^- conductive materials.

Oxyhydrides, where both oxide ions (O^{2-}) and H^- ions form an anion sublattice, allow

various compositions and crystal lattices, unlike metal hydrides; e.g., fluorites *Ln*HO (*Ln* = lanthanide),[6-9] mayenite $[Ca_{24}Al_{28}O_{64}]^{4+}\cdot H^-$,[10] ideal perovskites $ABO_{3-x}H_x$ (*A* = *AE*, Eu, *B* = Sc,[11] Ti,[12-14] V,[15] Cr[16]), layered perovskites $A_2B(H,O)_4$ (*A* = *Ln*, *AE*, *B* = Li,[17-19] Ti,[20] V,[15, 21] Mn,[22] Co,[23] Ni and Ru[24]) and hexagonal perovskite $BaVO_{3-x}H_x$.[25] We recently found the first (and so far, only) example of H^- conductive oxyhydrides $La_{2-x-y}Sr_{x+y}LiH_{1-x+y}O_{3-y}$ ($0 \le x \le 1$, $0 \le y \le 2$) with their function as an H^- solid electrolyte for electrochemical devices.[18] This Li-based series adopts layered perovskite (K_2NiF_4-type) structures in which the H^- ions preferentially occupy the equatorial anion sites and diffuse among them rather than via the apical sites. Given fast O^{2-} conduction via apical sites in isostructural oxides $Ln_2NiO_{4+\delta}$,[26-28] K_2NiF_4-type oxyhydrides with the different site selectivity of H^- might provide another H^- diffusion pathway, and perhaps, fast H^- conduction. Here, we report a successful synthesis of a new H^- conductive oxyhydride Ba_2ScHO_3 with K_2NiF_4-type structure where H^- anions selectively occupy the apical site in contrast to the reported Li-based series.

3.2 Experimental

3.2.1 Synthesis

Powder samples of Ba_2ScHO_3 were synthesized by solid-state reactions at high pressure using BaH_2 (Mitsuwa Chemical, 99.5%), BaO (Aldrich, 99.99%), and Sc_2O_3 (Aldrich, 99.999%) as starting reagents. A stoichiometric mixture of these reagents was thoroughly ground in an argon atmosphere and sealed in a BN sleeve. The sleeve was covered with a NaCl capsule inside a pyrophyllite cell fitted with a graphite heater. The cell was compressed to a pressure of 3 GPa using a cubic anvil press, heated at 800 °C for 30 min, and quenched to room temperature, followed by a slow release of pressure.

3.2.2 Characterization

Laboratory powder X-ray diffraction (XRD) measurements were performed using a diffractometer (MiniFlex 600, Rigaku) with Cu-K_α radiation. Since the samples were highly air-sensitive, they were loaded into an aluminum sample holder in an Ar-filled glovebox. Room-temperature powder synchrotron XRD (SXRD) measurements were performed at BL02B2 and BL19B2 in SPring-8 with a wavelength of λ = 0.5000 Å. The finely ground powder sample was loaded into a quartz capillary (inner diameter: 0.2 mm). The sealed capillary was rotated during measurements to reduce preferential orientation of the crystallites.

Time-of-flight powder neutron diffraction (ND) data of the sample (c.a. 0.5 g) loaded into a cylindrical vanadium cell (radius: 6 mm, height: 55 mm) were collected at room temperature using a SPICA diffractometer at J-PARC. The collected SXRD and ND profiles were analyzed by the Rietveld method using RIETAN-FP program[29] for the SXRD data and Z-Rietveld program[30] for the ND data. Crystal structures were illustrated by the VESTA program.[31]

3.2.3 First-principles calculations

First-principles total energy calculations were performed using the projector augmented wave method[32, 33] as implemented in the VASP code.[34-36] Exchange–correlation interactions were treated using the Perdew–Burke–Ernzerhof functional.[37] Configurations of the valence electrons in the PAW potentials are $5s^2$ $5p^6$ $6s^2$ for Ba, $3s^2$ $3p^6$ $3d^1$ $4s^2$ for Sc, $2s^2$ $2p^4$ for O, $1s^1$ for H. Cut-off energy for plane-wave basis sets was set as 500 eV. Lattice constants and atomic internal positions were fully optimized until all residual forces acting on atoms became smaller than 0.02 eV/Å. Symmetrically independent H/O configurations were searched using the `Spglib` library.[38] Brillouin-zone integration was performed with Monkhorst Pack grids[39] and k-point spacings less than $0.4 Å^{-1}$.

3.2.4 Conductivity

H^- conductivity was measured by AC impedance measurement under a H_2 or Ar flow at 200–340 °C with an applied frequency of 0.1–7 MHz using a Bio-Logic VSP-300 frequency response analyzer. The Pd reversible hydrogen electrode or the ion blocking Au electrode was deposited on both sides of the pelletized samples. The diameter (r) and thickness (t) of measured pellets are r = 3.62 mm, t = 1.58 mm for Pd-deposited one, and r = 3.66 mm, t = 1.44 mm for Au-one. The obtained impedance spectra were fitted with electrical equivalent circuits using the EC-Lab software.

3.3 Results and Discussion

3.3.1 Synthesis and structural analysis

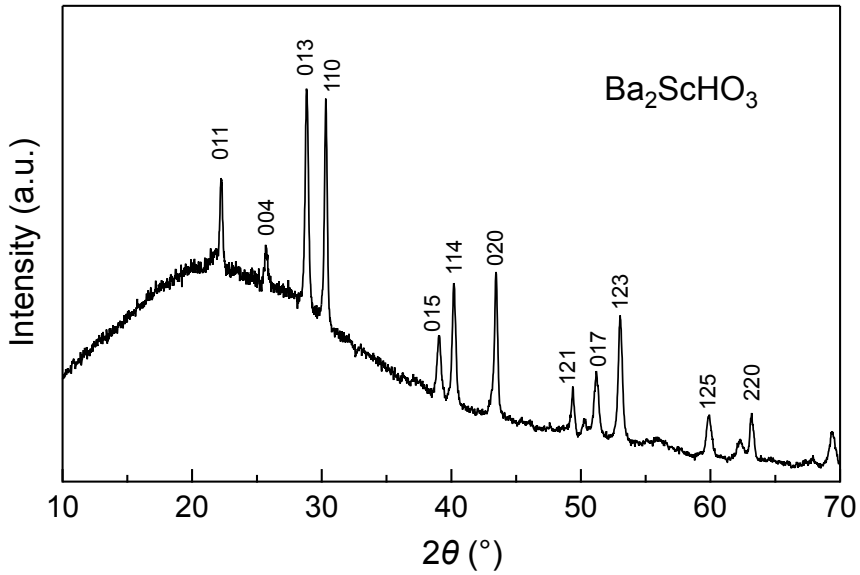

Figure 3.1 Laboratory XRD profile of $BaScHO_3$. The large background at lower angles was derived from the Kapton film attached to the sample holder for air-sensitive samples

The polycrystalline samples of Ba_2ScHO_3 were successfully synthesized by a solid-state reaction under high pressure. A stoichiometric mixture of BaH_2, BaO, and Sc_2O_3 was thoroughly ground and sealed in a cell, followed by heating at 800 °C under 3 GPa for 30 min. The laboratory X-ray diffraction (XRD) pattern (Figure 3.1) of the obtained off-white powder is mostly indexable with a tetragonal unit cell of a = ~4.16 Å and c = ~13.7 Å (Figure 3.1). The pattern of the tetragonal phase is similar to that of a K_2NiF_4-type oxyfluoride Ba_2ScO_3F where $[Ba_2OF]$ rock-salt layers and $[ScO_2]$ layers alternately stack along the c-axis.[40] Note that the product inevitably contains a small amount (10–20 wt%) of the residual raw materials or/and byproduct $BaScO_2H$[11]

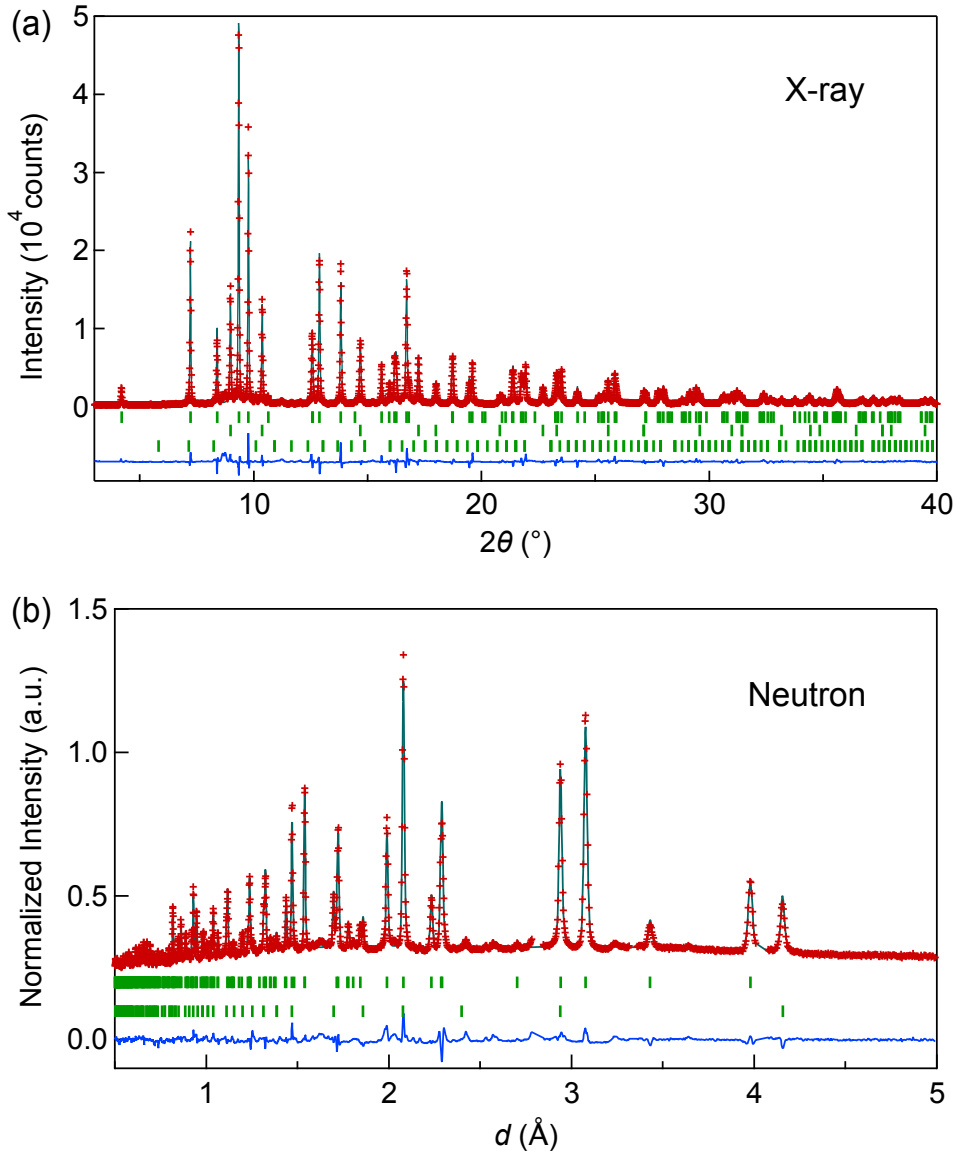

Figure 3.2 Rietveld refinements for (a) SXRD and (b) ND data of Ba_2ScHO_3. The red crosses, green solid line, and blue solid line represent the observed, calculated, and difference in intensities, respectively. Upper, middle, and lower green ticks for SXRD

The powder synchrotron XRD (SXRD) pattern contains peaks derived from the tetragonal phase together with small amounts of BaO and Sc_2O_3. We refined the data using the model based on a K_2NiF_4-type structure (space group *I*4/*mmm*), where Ba atoms were placed at the Wyckoff position 4*e*, Sc at 2*a*, O1 at 4*c*, and O2 at 4*e*. H^- anions were not considered here owing to their small electron number. The initial refinement converged well with the agreement factors of R_{wp} = 9.65% and R_p = 6.64% with somewhat large atomic displacement of Sc (U_{iso}(Sc) ~ 1.5 Å^2). By setting Sc at the 4*e* (0, 0, *z*) site with site-splitting occupation (*g* = 0.5), the U_{iso}(Sc) fell to a reasonable value of 0.16(5) Å^2 and the fitting was improved as R_{wp}

= 9.14%, R_p = 6.28% (Figure 3.2 (a) and Table 3.1). Remarkably, the estimated occupancy of the equatorial O1 site was 0.93(1), while that of the apical O2 site was 0.60(1), suggesting the preferred occupation of the vacancies or/and hydride ions at the apical site. It should be noted that this tendency was also observed in the initial refinement without the Sc site splitting. The meaning and validity of this site-splitting operation will be explained later.

Table 3.1 Structural parameters of Ba_2ScHO_3 from ND (upper) and SXRD (lower) data[a]

Atom	Site	*g*		*x*	*y*	*z*		B / Å^2	
Ba	4*e*	1.12)	0.982(1	0	0	2.18)	0.36309(17)	3.17)	0.829(14)
						0.36289(6)		0.97(2)	
Sc	4*e*	0.5		0	0	4.15)	0.01736(14)	5.14)	0.609(16)
						0.0167(3)		0.16(5)	
O1	4*c*	1	0.925(10)	0	0.5	0		6.14)	0.729(16)
								0.41(14)	
O2	4*e*	7.1(9)	0.5369	0	0	8.18)	0.16040(18)	9.1	0.45(6)
		0.599(14)				0.1578(8)		2.4(4)	
10.1	H 11.1e	4	12.1(7)	0.4631	13.1	0 14.1	0 15.1	0.16040(18)	16.1	0.45(6)
17.1	[a] *I*4/*mmm*; a = 4.154803(18) Å, c = 13.70967(12) Å, R_{wp} = 2.07%, R_p = 1.47%, S = 4.65, R_B = 5.05%, R_F = 7.12% for ND and a = 4.15498(8) Å, c = 13.6847(3) Å, R_{wp} = 9.14%, R_p = 6.28%, S = 2.59, R_B = 2.50%, R_F = 0.69% for SXRD.									

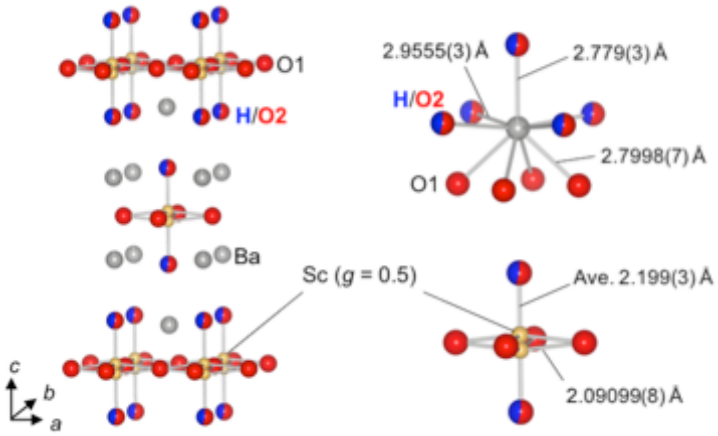

Figure 3.3 Crystal structure of Ba_2ScHO_3 and local coordination environments around Ba and Sc. Grey, orange, blue, and red balls represent Ba, Sc, H, and O atoms, respectively.

In order to clarify the anion configuration including hydrogen species, we also refined the powder neutron diffraction (ND) data. Although the measured sample contained $BaScO_2H$ rather than the raw materials, the lattice parameters were quite similar to those of samples used for SXRD measurement, allowing us to consider that they adopt identical structures. Based on the result of SXRD refinement, we assumed that the anion vacancies are fully occupied by hydrogen in accordance with the nominal composition. The initial refinement gave the occupation factor of the equatorial O1 site as 1.0013(12), leading us to fix the g(O1) value at unity. The following refinement was converged well, as shown in Figure 3.2b and Table 3.1 (R_{wp} = 2.07%, R_p = 1.47%), providing the estimated structure as shown in Figure 3.3. Notably, the refined occupancies of the apical site were g(O2)/g(H) = 0.5369(9)/0.4631(9), corresponding to occupation of H^- of nearly half. The bond valence sum (BVS) calculation[41, 42] applied to the refined structure gave values of +1.82 for Ba and +2.82 for Sc, which are consistent with the formal charges of Ba^{2+} and Sc^{3+}. Considering the charge neutrality condition, we conclude that the composition of the obtained K_2NiF_4-type oxyhydride is given by Ba_2ScHO_3, where H^- ions selectively occupy half of the apical sites.

3.3.2 First principles calculations

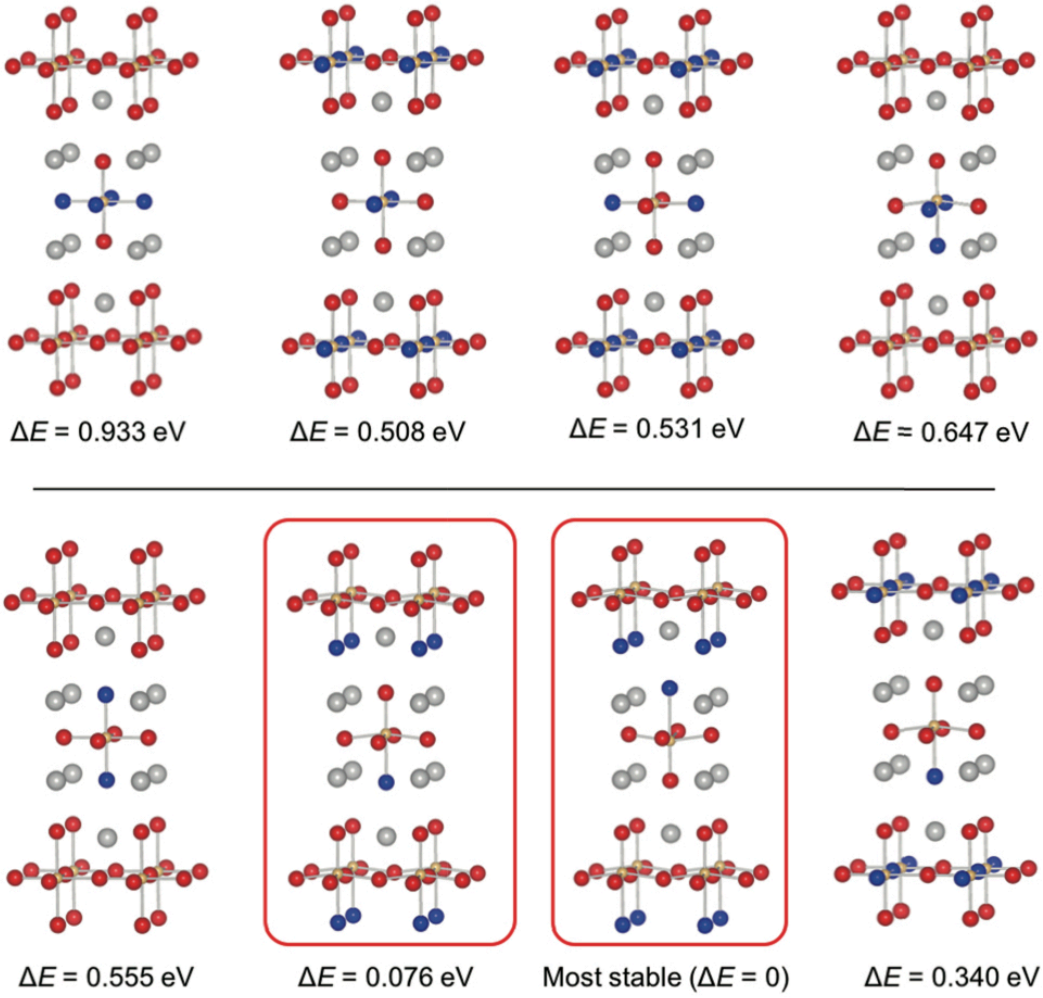

Figure 3.4 All symmetrically independent H/O configurations in the conventional unit cell of Ba_2ScHO_3 calculated in this study. The values of relative energies compared with the most stable configuration are shown.

The validity of the proposed structure with the site selectivity of H^- to the apical sites is also supported by first-principles calculations. Firstly, we calculated energies of symmetrically independent eight-anion configurations in the 1 × 1 × 1 conventional unit cell of Ba_2ScHO_3, yielding the result that structures where H^- are located only at the apical sites are significantly more stable compared to others ($\Delta E > 0.3$ eV per formula unit (eV/f.u.), Figure 3.4). Based on this result, energy calculations were performed using a 2 × 2 × 1 supercell with the condition that H^- occupation is limited to the apical sites (all 181 independent configurations).

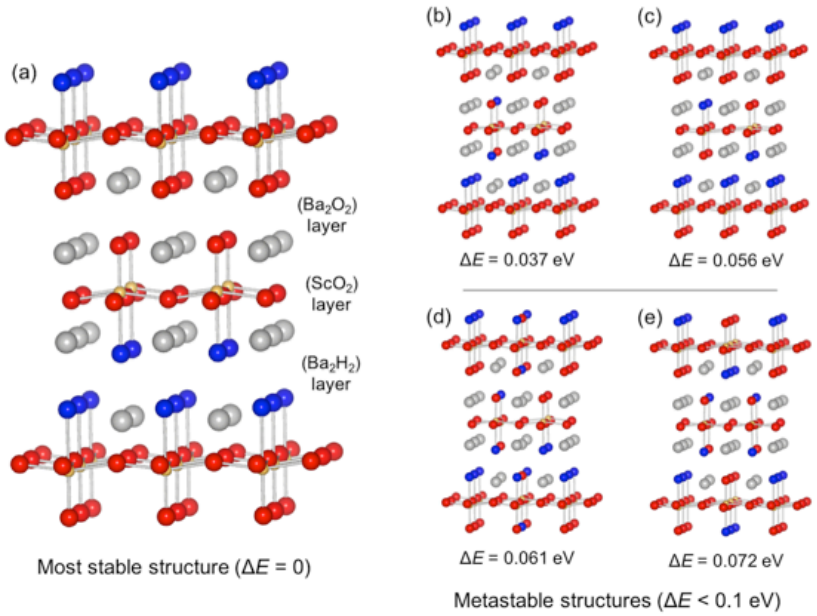

Figure 3.5 Most stable (ΔE = 0) and representative metasta-ble (ΔE < 0.1 eV/f.u.) structures for a 2 × 2 × 1 supercell of Ba_2ScHO_3 obtained by first-principles calculations. Grey, orange, blue, and red balls represent Ba, Sc, H, and O at-oms, respectively

Figure 3.5 shows the results; the structure (a) with the alternative stacking of $[Ba_2H_2]$ and $[Ba_2O_2]$ rock-salt layers across the $[ScO_2]$ layers along the *c*-axis is the most stable, while the stabilities of the structures (b-e) with the $[Ba_2(H,O)_2]$ rock-salt layers are comparable. In addition to the structures shown in Figure 3.5(b-e), eleven configurations where Δ*E* values are lower than 0.1 eV/f.u. were also found from our systematic first-principles calculations. These metastable structures can appear by thermodynamic fluctuation under high-temperature and high-pressure reaction conditions. Therefore, the refinement result using the polycrystalline data, i.e., the K_2NiF_4-type structure with a random distribution of H^- ions at the apical sites, is reasonable. In addition, the calculations indicate that the lengths of Sc-O bonds in the apical direction are shorter than those of Sc-H bonds and that Sc centers are shifted from the center of ScO_5H octahedra (Figure 3.6). The Sc displacement from the center of the ScO_5H octahedron toward the apical oxygen forms a ScO_5 pseudo-pyramid coordination, which requires the Sc site-splitting operation in the refinement. Such a metal off-centering in octahedra with mixed-anion coordination was also reported in K_2NiF_4-type oxyfluorides Sr_2CoO_3F[43] and Sr_2NiO_3F[44] with selective apical fluoride ions.

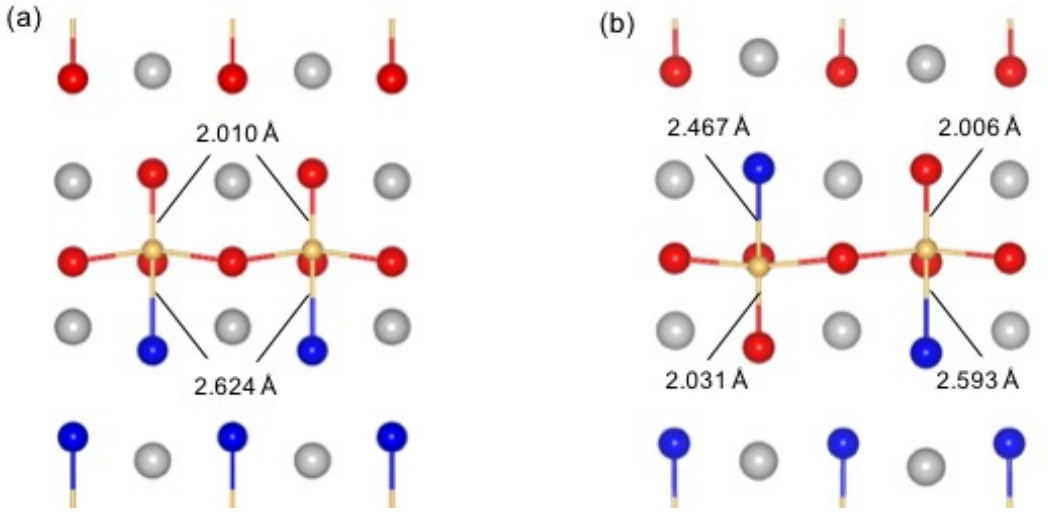

Figure 3.6 Optimized coordination environment of ScO_5H in the supercells of Ba_2ScO_3H. Left and right images correspond to the supercells of Figures 3.6 (a) and (b), respectively.

Such site selectivity of H^- at apical sites is rare in K_2NiF_4-type oxyhydrides; most of the reported compounds including $LaSrCoO_3H_{0.7}$,[23] Sr_2VO_3H,[15, 21] $LaSrMnO_{3.3}H_{0.7}$,[22] $La_{2-x-y}Sr_{x+y}LiH_{1-x+y}O_{3-y}$, and $LaSr_3NiRuO_4H_4$[24] adopted structures with selective (or preferred) equatorial H^-. Very recently, Hernandez *et al.* reported $Sr_2TiO_{3.875}H_{0.14}$ with a small amount of H^- at the apical sites.[20] The unique apical H^- with a sizable amount of Ba_2ScHO_3 could be explained by Pauling's second crystal rule (electrostatic valence rule), which was widely applied for K_2NiF_4-type mixed-anion oxides by Fuertes *et al.*[46] According to this rule, a more/less charged anion prefers a site possessing a larger/smaller bond strength sum. In Ba_2ScHO_3, the apical site surrounded by one more charged Sc^{3+} and five less charged Ba^{2+} is more suitable for H^- (less charged anion) than the equatorial site surrounded by two more charged Sc^{3+} and four less charged Ba^{2+}. In contrast, H^- conductive $La_{2-x-y}Sr_{x+y}LiH_{1-x+y}O_{3-y}$ adopts the preferred equatorial H^- owing to the less charged Li^+ at the $Li(H,O)_6$ octahedra. This tendency means that H^-/O^{2-} arrangements in oxyhydrides composed of relatively electropositive cations could be tuned from an electrostatic viewpoint. Note that oxyhydrides with *d*-electrons do not necessarily follow this rule owing to the ligand field effect or/and the small electronegativity of hydrogen.[22]

3.3.3 Ionic conductivity

Ionic conductivity of the prepared pellet with Pd electrodes was evaluated by AC impedance measurement at 200–340 °C under flowing H_2 gas. The obtained impedance plots (collected at 300 ºC is shown in Figure 3.7a) could be regarded as a combination of two

components; a clear semicircle in the high-frequency range and a part in the low-frequency range, which correspond to responses from the mixture of bulk/grain boundary and the electrode, respectively. We fitted the bulk/grain boundary part by using an equivalent circuit to estimate its resistance at each temperature, yielding the Arrhenius plots as shown in Figure 3.7c. Since the possible impure phases of BaO, Sc_2O_3, and $BaScO_2H$ (described later) hardly exhibit ion conduction at the measured temperature range, the major phase of Ba_2ScHO_3 is dominantly responsible for the ionic conduction. The intrinsic conductivity of Ba_2ScHO_3 might be somewhat underestimated due to these insulating impurities. Note that XRD profile after the measurement showed that the K_2NiF_4-type structure remained (Figure 3.8).

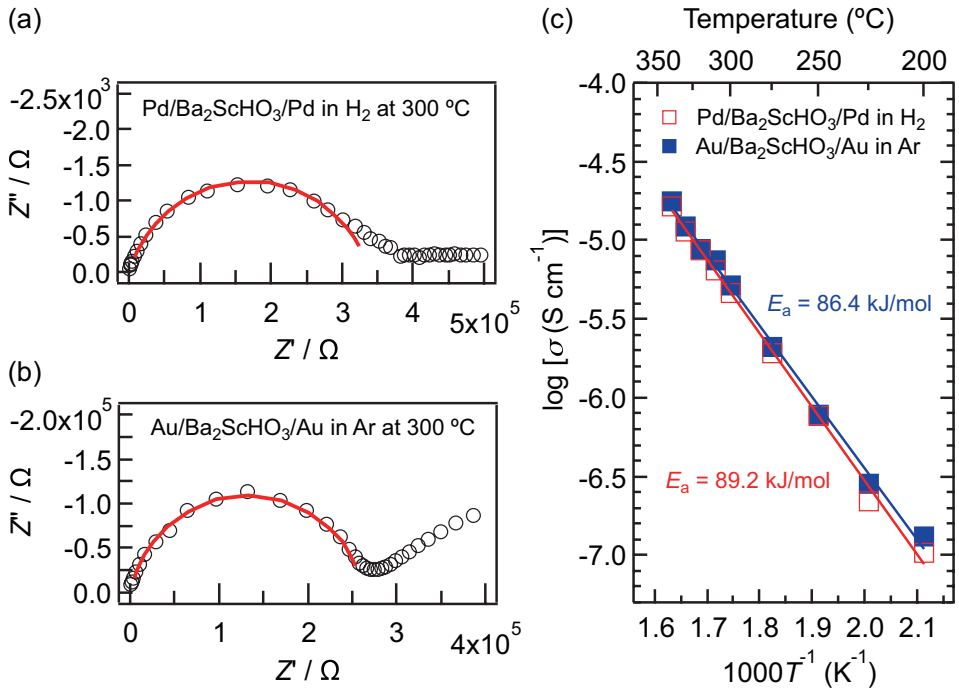

Figure 3.7 Cole–Cole plots for Ba_2ScHO_3 measured with (a) Pd electrodes under flowing H_2 gas and (b) Au electrodes under flowing Ar gas. (c) Arrhenius plots of the total conductivity (bulk + grain boundary). Filled red-open and blue-closed square represent those measured using Pd and Au electrodes, respectively

In order to investigate the conducting nature, we also performed impedance measurement using blocking Au electrodes under Ar flow (Figure 3.7b). A spike derived from the ion blocking electrode was observed on the low frequency range, unlike the case where the Pd electrode was used in H_2 atmosphere. The conductivity at each temperature in Ar atmosphere was almost the same value as when the Pd electrode was used under H_2 atmosphere, and as a result, quite similar activation energies were estimated from obtained Arrhenius plots (Figure 3.7c). The non-dependence of conductivity on the presence or absence

of H_2 gas shows that electron conduction does not occur even under Ar atmosphere (low H_2 partial pressure), suggesting that Ba_2ScHO_3 is a pure ionic conductor at the measurement temperature range. In terms of K_2NiF_4-type oxyhydrides $La_{2-x-y}Sr_{x+y}LiH_{1-x+y}O_{3-y}$, pure H^- conduction was confirmed by all-solid-state cell experiments, and calculation studies for $La_{2-x-y}Sr_{x+y}LiH_{1-x+y}O_{3-y}$ and Ln_2LiHO_3 (*Ln* = Pr, Nd) showed that the activation barriers of H^- diffusion are significantly smaller than those of O^{2-} diffusion.[19, 47-48] From these, it is reasonable to consider that the ionic conduction in Ba_2ScHO_3 is dominantly derived from H^- diffusion. A recent study on point defect formation energies and anionic conduction mechanisms using first-principles calculations by Kuwabara *et. al.* also stated hydride ion as dominant charge carrier in Ba_2ScHO_3.[48]

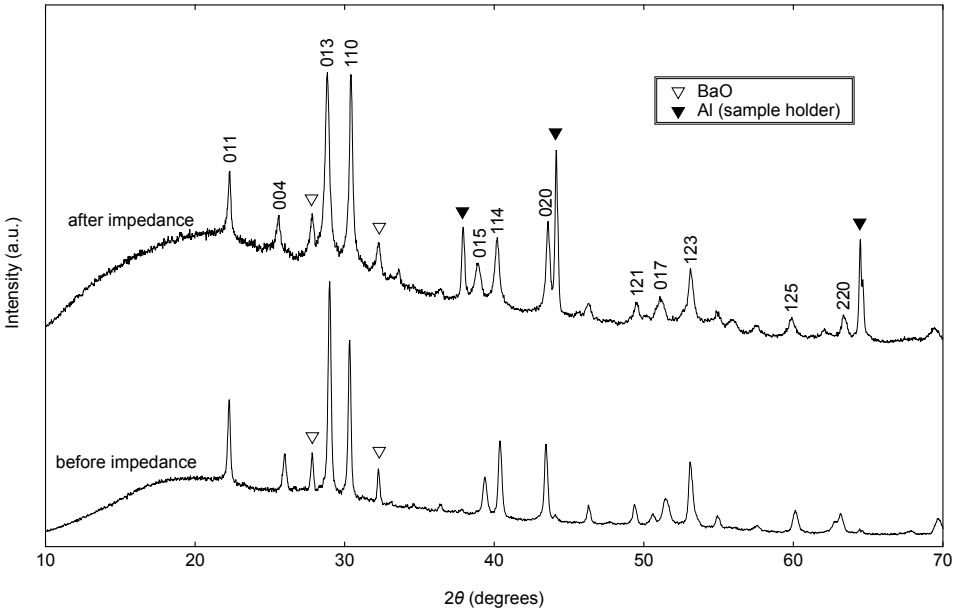

Figure 3.8 XRD profile of Ba_2ScHO_3 before and after impedance measurement. The peaks with the open and closed triangle represent those of BaO and Al (sample holder), respectively. The sample lot is different from one for Figure 3.1

The H^- conductivity at 300 °C reached 5.2×10^{-6} S cm^{-1} (activation energy ~86.4 kJ mol^{-1}), which is comparable to those of Ln_2LiH_3O and $LaSrLiH_2O_2$. In contrast, notably, the conductivity of Ba_2ScHO_3 is much higher than that of an ideal perovskite oxyhydride $BaScO_2H$[11], ~7×10^{-8} S cm^{-1} at 300 °C (Figure 3.9), though the H^- concentration for the total anions of the former (25%) is smaller than that of the latter (33%). Given that O^{2-} is less mobile at the measured temperature range (≤ 300 °C), the superiority of Ba_2ScHO_3 indicates that the apical H^- ions diffuse preferentially within the rock-salt layer, where H^- concentration is

enhanced to 50%, rather than by three-dimensional diffusion. This increase of carrier concentration at the diffusion pathway could be because of site selectivity of H^-, allowing us to expect that the theoretically predicted most stable structure of Ba_2ScHO_3 with the Ba_2H_2 rock-salt layer (Figure 3.5a) might show much higher conductivity.

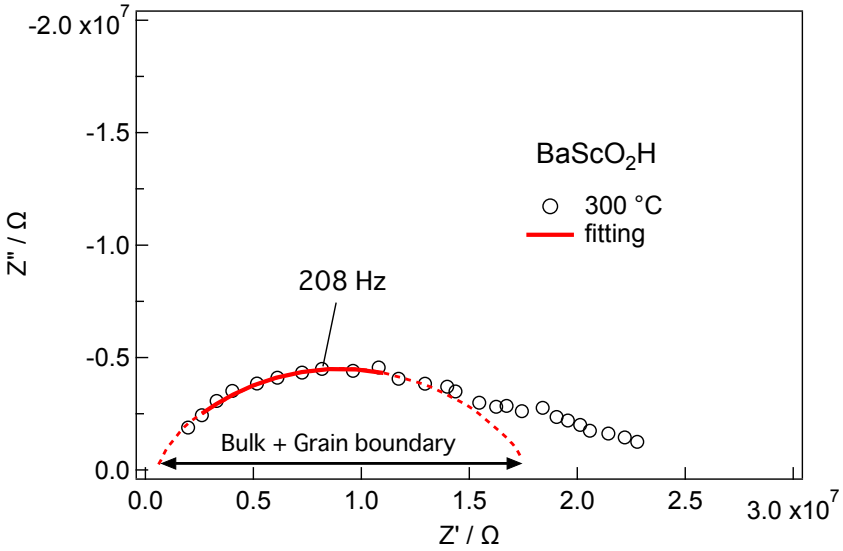

Figure 3.9 Impedance plot of $BaScO_2H$ at 300 °C.

3.4 Conclusion

We obtained a new oxyhydride Ba_2ScHO_3 that adopts the K_2NiF_4-type structure with preferred apical H^- ions and observed its H^- conductivity as superior to that of an ideal perovskite $BaScO_2H$. Tuning the site selectivity of H^-, according to the electrostatic valence rule, should help to design the H^- diffusion pathway in layered oxyhydrides. An increased H^- concentration at the apical sites by appropriate element substitutions, a preferred anion configuration and optimized hydride ion diffusion pathways can help to further enhance the hydride ion conduction through rock salt layers in K_2NiF_4-type oxyhydrides.

References

[1] Andresen, A.; Maeland, A.; Slotfeldt-Ellingsen, D. Calcium hydride and deuteride studied by neutron diffraction and NMR. *J. Solid State Chem.* **1977,** 20, 93-101.

[2] Wegner, B.; Essmann, R.; Bock, J.; Jacobs, H.; Fischer, P. Structure and hydrogen ion-ionic-conductivity of barium hydride nitride, $Ba_2H(D)N$. *Eur. J. Solid State Inorg. Chem.* **1992,** 29, 1217-1227.

[3] Altorfer, F.; Buhrer, W.; Winkler, B.; Coddens, G.; Essmann, R.; Jacobs, H. H^--jump diffusion in barium-nitride-hydride Ba_2NH. *Solid State Ionics* **1994,** 70-71, 272-277.

[4] Verbraeken, M. C.; Suard, E.; Irvine, J. T. S. Structural and electrical properties of calcium and strontium hydrides. *J. Mater. Chem.* **2009,** 19, 2766-2770.

[5] Verbraeken, M. C.; Cheung, C.; Suard, E.; Irvine, J. T. High H^- ionic conductivity in barium hydride. *Nat Mater* **2015,** 14, 95-100.

[6] Ueda, J.; Matsuishi, S.; Tokunaba, T.; Tanabe, S. Preparation, Electronic Structure of Gadolinium Oxyhydride and Low-energy 5d Excitation Band for Green Luminescence of Doped Tb^{3+} Ions. *J. Mater. Chem. C* **2018,** 6, 7541-7548.

[7] Yamashita, H.; Broux, T.; Kobayashi, Y.; Takeiri, F.; Ubukata, H.; Zhu, T.; Hayward, M. A.; Fujii, K.; Yashima, M.; Shitara, K.; Kuwabara, A.; Murakami, T.; Kageyama, H. Chemical Pressure-Induced Anion Order-Disorder Transition in LnHO Enabled by Hydride Size Flexibility. *J. Am. Chem. Soc.* **2018,** 140, 11170-11173.

[8] Brice, J.; Malaman, B.; Evrard, O. Synthesis, structural study and electrical properties of hydride Oxides: LaHO, $LaH_{1+2x}O_{1-x}$ and $LaH_{1+y}O_{1-x}$ ($y = 2x$). *Inorg. Chim. Acta* **1984,** 94, 123.

[9] Widerøe, M.; Fjellvåg, H.; Norby, T.; Willy Poulsen, F.; Willestofte Berg, R. NdHO, a novel oxyhydride. *J. Solid State Chem.* **2011,** 184, 1890-1894.

[10] Hayashi, K.; Matsuishi, S.; Kamiya, T.; Hirano, M.; Hosono, H. Light-induced conversion of an insulating refractory oxide into a persistent electronic conductor. *Nature* **2002,** 419, 462.

[11] Goto, Y.; Tassel, C.; Noda, Y.; Hernandez, O.; Pickard, C. J.; Green, M. A.; Sakaebe, H.; Taguchi, N.; Uchimoto, Y.; Kobayashi, Y.; Kageyama, H. Pressure-Stabilized Cubic Perovskite Oxyhydride $BaScO_2H$. *Inorg. Chem.* **2017,** 56, 4840-4845.

[12] Kobayashi, Y.; Hernandez, O. J.; Sakaguchi, T.; Yajima, T.; Roisnel, T.; Tsujimoto, Y.; Morita, M.; Noda, Y.; Mogami, Y.; Kitada, A.; Ohkura, M.; Hosokawa, S.; Li, Z.; Hayashi, K.; Kusano, Y.; Kim, J.; Tsuji, N.; Fujiwara, A.; Matsushita, Y.; Yoshimura,

K.; Takegoshi, K.; Inoue, M.; Takano, M.; Kageyama, H. An oxyhydride of $BaTiO_3$ exhibiting hydride exchange and electronic conductivity. *Nat Mater* **2012,** 11, 507-511.

[13] Sakaguchi, T.; Kobayashi, Y.; Yajima, T.; Ohkura, M.; Tassel, C.; Takeiri, F.; Mitsuoka, S.; Ohkubo, H.; Yamamoto, T.; Kim, J.; Tsuji, N.; Fujihara, A.; Matsushita, Y.; Hester, J.; Avdeev, M.; Ohoyama, K.; Kageyama, H. Oxyhydrides of (Ca,Sr,Ba)TiO_3 perovskite solid solutions. *Inorg. Chem.* **2012,** 51, 11371-11376.

[14] Yamamoto, T.; Yoshii, R.; Bouilly, G.; Kobayashi, Y.; Fujita, K.; Kususe, Y.; Matsushita, Y.; Tanaka, K.; Kageyama, H. An antiferro-to-ferromagnetic transition in $EuTiO_{3-x}H_x$ induced by hydride substitution. *Inorg. Chem.* **2015,** 54, 1501-1507.

[15] Denis Romero, F.; Leach, A.; Moller, J. S.; Foronda, F.; Blundell, S. J.; Hayward, M. A. Strontium vanadium oxide-hydrides: "square-planar" two-electron phases. *Angew. Chem. Int. Ed.* **2014,** 53, 7556-7559.

[16] Tassel, C.; Goto, Y.; Kuno, Y.; Hester, J.; Green, M.; Kobayashi, Y.; Kageyama, H. Direct synthesis of chromium perovskite oxyhydride with a high magnetic-transition temperature. *Angew. Chem. Int. Ed.* **2014,** 53, 10377-10380.

[17] Schwarz, H. Neuartige Hydrid-Oxide der seltenen Erden : Ln_2LiHO_3 mit Ln = La, Ce, Pr und Nd. *Thesis, Univ. Karlsrühe* **1991**.

[18] Kobayashi, G.; Hinuma, Y.; Matsuoka, S.; Watanabe, A.; Iqbal, M.; Hirayama, M.; Yonemura, M.; Kamiyama, T.; Tanaka, I.; Kanno, R. Pure H^- conduction in oxyhydrides. *Science* **2016,** 351, 1314-1317.

[19] Iwasaki, Y.; Matsui, N.; Suzuki, K.; Hinuma, Y.; Yonemura, M.; Kobayashi, G.; Hirayama, M.; Tanaka, I.; Kanno, R. Synthesis, crystal structure, and ionic conductivity of hydride ion-conducting Ln_2LiHO_3 (Ln = La, Pr, Nd) oxyhydrides. *J. Mater. Chem. A* **2018,** 6, 23457-23463.

[20] Hernandez, O. J.; Geneste, G.; Yajima, T.; Kobayashi, Y.; Okura, M.; Aidzu, K.; Tassel, C.; Paofai, S.; Swain, D.; Ritter, C.; Kageyama, H. Site Selectivity of Hydride in Early-Transition-Metal Ruddlesden-Popper Oxyhydrides. *Inorg. Chem.* **2018,** 57, 11058-11067.

[21] Bang, J.; Matsuishi, S.; Hiraka, H.; Fujisaki, F.; Otomo, T.; Maki, S.; Yamaura, J.; Kumai, R.; Murakami, Y.; Hosono, H. Hydrogen ordering and new polymorph of layered perovskite oxyhydrides: $Sr_2VO_{4-x}H_x$. *J. Am. Chem. Soc.* **2014,** 136, 7221-7224.

[22] Tassel, C.; Goto, Y.; Watabe, D.; Tang, Y.; Lu, H.; Kuno, Y.; Takeiri, F.; Yamamoto, T.; Brown, C. M.; Hester, J. High-Pressure Synthesis of Manganese Oxyhydride with Partial Anion Order. *Angew. Chem.* **2016,** 128, 9819-9822.

[23] Hayward, M. A.; Cussen, E. J.; Claridge, J. B.; Bieringer, M.; Rosseinsky, M. J.; Kiely, C. J.; Blundell, S. J.; Marshall, I. M.; Pratt, F. L. The hydride anion in an extended transition metal oxide array: $LaSrCoO_3H_{0.7}$. *Science* **2002,** 295, 1882-1884.

[24] Jin, L.; Lane, M.; Zeng, D.; Kirschner, F. K.; Lang, F.; Manuel, P.; Blundell, S. J.; McGrady, J. E.; Hayward, M. A. $LaSr_3NiRuO_4H_4$: A 4d Transition-Metal Oxide-Hydride Containing Metal Hydride Sheets. *Angew. Chem.* **2018,** 130, 5119-5122.

[25] Yamamoto, T.; Shitara, K.; Kitagawa, S.; Kuwabara, A.; Kuroe, M.; Ishida, K.; Ochi, M.; Kuroki, K.; Fujii, K.; Yashima, M.; Brown, C. M.; Takatsu, H.; Tassel, C.; Kageyama, H. Selective Hydride Occupation in $BaVO_{3-x}H_x$ ($0.3 \leq x \leq 0.8$) with Face- and Corner-Shared Octahedra. *Chem. Mater.* **2018,** 30, 1566-1574.

[26] Skinner, S. J.; Kilner, J. A. Oxygen diffusion and surface exchange in $La_{2-x}Sr_xNiO_{4+\delta}$. *Solid State Ionics* **2000,** 135, 709-712.

[27] Bassat, J. M.; Odier, P.; Villesuzanne, A.; Marin, C.; Pouchard, M. Anisotropic ionic transport properties in $La_2NiO_{4+\delta}$ single crystals. *Solid State Ionics* **2004,** 167, 341-347.

[28] Yashima, M.; Enoki, M.; Wakita, T.; Ali, R.; Matsushita, Y.; Izumi, F.; Ishihara, T. Structural Disorder and Diffusional Pathway of Oxide Ions in a Doped Pr_2NiO_4-Based Mixed Conductor. *J. Am. Chem. Soc.* **2008,** 130, 2762-2763.

[29] Izumi, F.; Momma, K. Three-Dimensional Visualization in Powder Diffraction. *Solid State Phenomena* **2007,** 130, 15-20.

[30] Oishi, R.; Yonemura, M.; Nishimaki, Y.; Torii, S.; Hoshikawa, A.; Ishigaki, T.; Morishima, T.; Mori, K.; Kamiyama, T. Rietveld analysis software for J-PARC. *Nuclear Instruments and Methods in Physics Research Section A: Accelerators, Spectrometers, Detectors and Associated Equipment* **2009,** 600, 94-96.

[31] Momma, K.; Izumi, F. VESTA 3 for three-dimensional visualization of crystal, volumetric and morphology data. *J. Appl. Crystallogr.* **2011,** 44, 1272-1276.

[32] Blöchl, P. E. Projector augmented-wave method. *Phys. Rev. B* **1994,** 50, 17953-17979.

[33] Kresse, G.; Joubert, D. From ultrasoft pseudopotentials to the projector augmented-wave method. *Phys. Rev. B* **1999,** 59, 1758-1775.

[34] Kresse, G.; Hafner, J. Ab initio molecular dynamics for liquid metals. *Phys. Rev. B* **1993,** 47, 558-561.

[35] Kresse, G.; Furthmüller, J. Efficient iterative schemes for ab initio total-energy calculations using a plane-wave basis set. *Phys. Rev. B* **1996,** 54, 11169-11186.

[36] Kresse, G.; Furthmüller, J. Efficiency of ab-initio total energy calculations for metals and semiconductors using a plane-wave basis set. *Computational Materials Science* **1996,** 6, 15-50.

[37] Perdew, J. P.; Burke, K.; Ernzerhof, M. Generalized Gradient Approximation Made Simple. *Phys. Rev. Lett.* **1996,** 77, 3865-3868.

[38] Togo, A.; Tanaka, I. `Spglib`: a software library for crystal symmetry search. *arXiv:1808.01590* **2018**.

[39] Monkhorst, H. J.; Pack, J. D. Special points for Brillouin-zone integrations. *Phys. Rev. B* **1976,** 13, 5188-5192.

[40] Needs, R. L.; Weller, M. T.; Scheler, U.; Harris, R. K. Synthesis and structure of Ba_2InO_3X (X = F, Cl, Br) and Ba_2ScO_3F; oxide/halide ordering in K_2NiF_4-type structures. *J. Mater. Chem.* **1996,** 6, 1219-1224.

[41] Brown, I.; Altermatt, D. Bond-valence parameters obtained from a systematic analysis of the inorganic crystal structure database. *Acta Crystallogr. Sect. B: Struct. Sci.* **1985,** 41, 244-247.

[42] Brese, N.; O'keeffe, M. Bond-valence parameters for solids. *Acta Crystallogr. Sect. B: Struct. Sci.* **1991,** 47, 192-197.

[43] Tsujimoto, Y.; Li, J. J.; Yamaura, K.; Matsushita, Y.; Katsuya, Y.; Tanaka, M.; Shirako, Y.; Akaogi, M.; Takayama-Muromachi, E. New layered cobalt oxyfluoride, Sr_2CoO_3F. *Chem. Commun.* **2011,** 47, 3263-3265.

[44] Tsujimoto, Y.; Yamaura, K.; Uchikoshi, T. Extended Ni(III) Oxyhalide Perovskite Derivatives: Sr_2NiO_3X (X = F, Cl). *Inorg. Chem.* **2013,** 52, 10211-10216.

[45] Tobías, G.; Beltrán-Porter, D.; Lebedev, O. I.; Van Tendeloo, G.; Rodríguez-Carvajal, J.; Fuertes, A. Anion Ordering and Defect Structure in Ruddlesden-Popper Strontium Niobium Oxynitrides. *Inorg. Chem.* **2004,** 43, 8010-8017.

[46] Fjellvåg, Ø. S.; Armstrong, J.; Vajeeston, P.; Sjåstad, A. O. New Insights into Hydride Bonding, Dynamics, and Migration in La_2LiHO_3 Oxyhydride. *J. Phys. Chem. Let.* **2018,** 9, 353-358.

[47] Liu, X.; Bjørheim, T. S.; Haugsrud, R. Formation of defects and their effects on hydride ion transport properties in a series of K_2NiF_4-type oxyhydrides. *J. Mater. Chem. A* **2018,** 6, 1454-1461.

[48] Kuwabara, A.; Takeiri, F.; Nawaz, H.; Kobayashi, G. First-principles calculations of point defect formation and anion diffusion mechanism in oxyhydride Ba_2ScHO_3. **2020**, *ChemRxiv*, 10.26434/chemrxiv.12121254.v1.

Chapter 4

Enhanced H^- Conductivity by Anion Ordering in a Layered Perovskite Oxyhydride

Abstract:

The new layered perovskite oxyhydride Ba_2YHO_3 was synthesized by high pressure synthesis. Powder X-ray and neutron diffraction experiments revealed that in Ba_2YHO_3 the ordered H^- and O^{2-} anions form hydrogen-rich $[Ba_2H_2]$ rock-salt layers wherein H^-conduction is allowed. The conductivity reached 0.1 $mS \cdot cm^{-1}$ at 350 °C, which is higher than that of isostructural Ba_2ScHO_3 with the anion-disordered $[Ba_2HO]$ layers

4.1 Introduction

The mobility of ions in solids depends on the basic characteristics of each ionic species. Monovalent and soft (large polarizability) ions are generally favorable for diffusion compared with multivalent and hard (small polarizability) ions. In general, ionic conductors, the latter immobile species form crystal sublattices suitable for the conduction of the former mobile ones. For example, cation conductors such as $Na_{1+x}Zr_2Si_xP_{3-x}O_{12}$ (NASICON)[1] and $Li_{10}GeP_2S_{12}$ (LGPS)[2] include polyanion units of ZrO_6 octahedra and $(Si/P/Ge)(O/S)_4$ tetrahedra that enclose the network of interconnected paths of carrier Na^+/Li^+ ions, while for anion conductors, fast F^- diffusion in ß-$PbSnF_4$ is achieved at interlayers consisting of ordered Pb and Sn ions[3-5].

Hydride ion conduction in oxyhydrides is a new field in anion conduction and is also a representative case wherein the arrangement of mobile H^- and immobile O^{2-} crucially affects the conduction. In layered perovskites (K_2NiF_4-type) $Ln_{2-x-y}Sr_{x+y}LiH_{1-x+y}O_{3-y}$ (*Ln* = La, Nd, Pr)[6, 7], H^- ions selectively occupied the equatorial anion sites and formed conduction paths in the perovskite layers. In fluorite-type *Ln*HO (*Ln* = La, Nd, Gd, Er), only the H^-/O^{2-} ordered structures (*Ln* = La, Nd) showed H^- conduction while the disordered structures (*Ln* = Gd, Er) had no ionic conduction.[8] Moreover, hydrogen-rich $LaH_{3-2x}O_x$ exhibited fast H^- conduction (2.6×10^{-2} $S \cdot cm^{-1}$ at 342 °C) via

interstitial anionic sites unoccupied by O^{2-} ions.[9] These examples indicate that the design of anion ordering manner is crucial for development of H^- conduction in oxyhydrides.

We recently reported a layered perovskite oxyhydride Ba_2ScHO_3 with partial anion ordering wherein H^- ions occupy the apical sites rather than the equatorial sites to form $[Ba_2HO]$ rock-salt layers (Figure 4.1a), in contrast to the above mentioned $Ln_{2-x-y}Sr_{x+y}LiH_{1-x+y}O_{3-y}$ series[10]. Given fast ion conduction in rock-salt layers is known in O^{2-}/e^- mixed conductors $Ln_2NiO_{4+\delta}$,[11-13] the H^- conduction in this layer would be interesting, but the conductivity of Ba_2ScHO_3 was suppressed (5.2×10^{-6} $S \cdot cm^{-1}$ at 300 °C). A subsequent theoretical study pointed out that the slow (nearly immobile) O^{2-} migration at the diffusion path would inhibit the smooth H^- diffusion[14]. In this communication, we show the high-pressure synthesis of a yttrium-based oxyhydride Ba_2YHO_3, which adopts a structure with complete H^-/O^{2-} anion ordering to form $[Ba_2H_2]$ rock-salt layers (Figure 4.1b) where no O^{2-} ions lie in, and its higher conductivity compared to Ba_2ScHO_3.

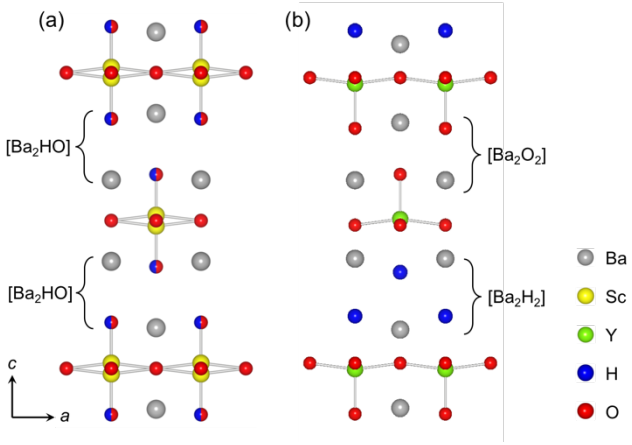

Figure 4.1. Crystal structures of layered perovskite oxyhydrides. a) Ba_2ScHO_3,[7] b) Ba_2YHO_3 (this work).

4.2 Experimental

Polycrystalline samples of Ba_2YHO_3 oxyhydride were synthesized by solid state reaction under high pressure, using BaH_2 (Mitsuwa Chemical, 99.5%), BaO (Aldrich, 99.99%), Y_2O_3 (Aldrich, 99.999%), and NaH (Aldrich, 95%). The reagents were weighed in an Ar filled glovebox, thoroughly mixed in a planetary ball mill, and sealed in a NaCl capsule inside a pyrophyllite cell with a graphite heater. The cell was heated at 700–1000 °C under 2–4 GPa for 1 h.

4.2.2 Characterization

Structural characterization of the samples was carried out with an X-ray powder diffractometer (Miniflex600, Rigaku) with Cu-Kα radiation. Since the oxyhydride compounds were highly air-sensitive, the powder samples were loaded on an aluminum holder in an Ar filled glovebox. Synchrotron X-ray diffraction (SXRD) data was collected at room temperature using a high-resolution angle-dispersive type X-ray diffractometer (BL02B2) installed at SPring-8. The wavelength of the incident beam was 0.8 Å. The powder samples were sealed in a Lindemann glass capillary (ϕ 0.3 mm) that was rotated during the measurement to reduce the preferential orientation. Neutron diffraction (ND) measurement at room temperature was carried out using a time-of-flight (TOF) neutron SPICA powder diffractometer in-stalled at J-PARC. Powder samples were loaded in a cylindrical vanadium cell. RIETAN-FP and Z-Rietveld programs[15,16] were used to refine the SXRD and ND data, respectively. Crystal structures were illustrated using VESTA software[17]. Thermogravimetric analysis (TGA) was conducted under flowing Ar gas (100 mL/min) with a Rigaku Thermo plus EVO2 installed in an Ar-filled glove box.

4.2.3 First-principles calculations

First-principles total energy calculations were performed using the projector augmented wave method[18,19] as implemented in the VASP code[20–21]. Exchange-correlation interactions of electrons were treated using the Perdew-Burke-Ernzerhof functional (PBE) based on the generalized gradient approximation (GGA)[20]. Configurations of the valence electrons in the PAW potentials are $5s^2\ 5p^6\ 6s^2$ for Ba, $4s^2\ 4p^6\ 4d^1\ 5s^2$ for Y, $2s^2\ 2p^4$ for O, and $1s^1$ for H. The cut-off energy for plane-wave basis sets was set to 500 eV. Lattice constants and atomic internal positions were fully optimized until all residual forces acting on atoms were less than 0.02 eV/Å. Symmetrically independent H/O configurations were identified

using the Spglib library[24]. Brillouin-zone integration was performed with Monkhorst Pack grids[25] and k-point spacings less than 0.4 $Å^{-1}$.

4.2.4 Conductivity

Ionic conductivity of the oxyhydrides was measured by the AC impedance method using a pellet sample obtained by high pressure synthesis. The diameter (r) and thickness (t) of measured pellets were r = 3.95 mm and t = 1.35 mm. The sample was coated with molybdenum electrodes sputtered on both sides under H_2 gas flow. The data was collected during heating and cooling cycles at the temperature range of 180–400 °C with an applied frequency range of 0.1 Hz to 35 MHz using an MTZ-35 frequency response analyzer. EC-Lab software was used to fit the spectra with electrically equivalent circuits. The DC electric conductivity of Ba_2YHO_3 was performed at 320 ºC under flowing H_2 gas using the sintered pellet with hydrogen blocking Mo electrodes.

4.3 Result and Discussion

4.3.1 Synthesis and structural analysis

The high-pressure synthesis of a barium yttrium oxyhydride was performed using a mixture of raw materials, BaH_2, BaO, and Y_2O_3, with a molar ratio of 1:3:1 (i.e. a stoichiometric ratio for Ba_2YHO_3) to yield the tetragonal phase (a ~ 4.38 Å, c ~ 13.8 Å) with oxides of BaO and BaY_2O_4. Alternatively, when minimal NaH was added to the raw materials, the tetragonal phase of the product remarkably increased. Through the optimization of the molar ratio of the four raw materials, sintering temperature (700–1000 °C), and applied pressure (2–4 GPa), we found that the purity of the tetragonal phase was maximized when reacted at 800 °C under 4 GPa with BaH_2:BaO:Y_2O_3:NaH =0.55:1.45:0.45:0.1. The obtained powder sample is off-white suggesting absence of free electrons.

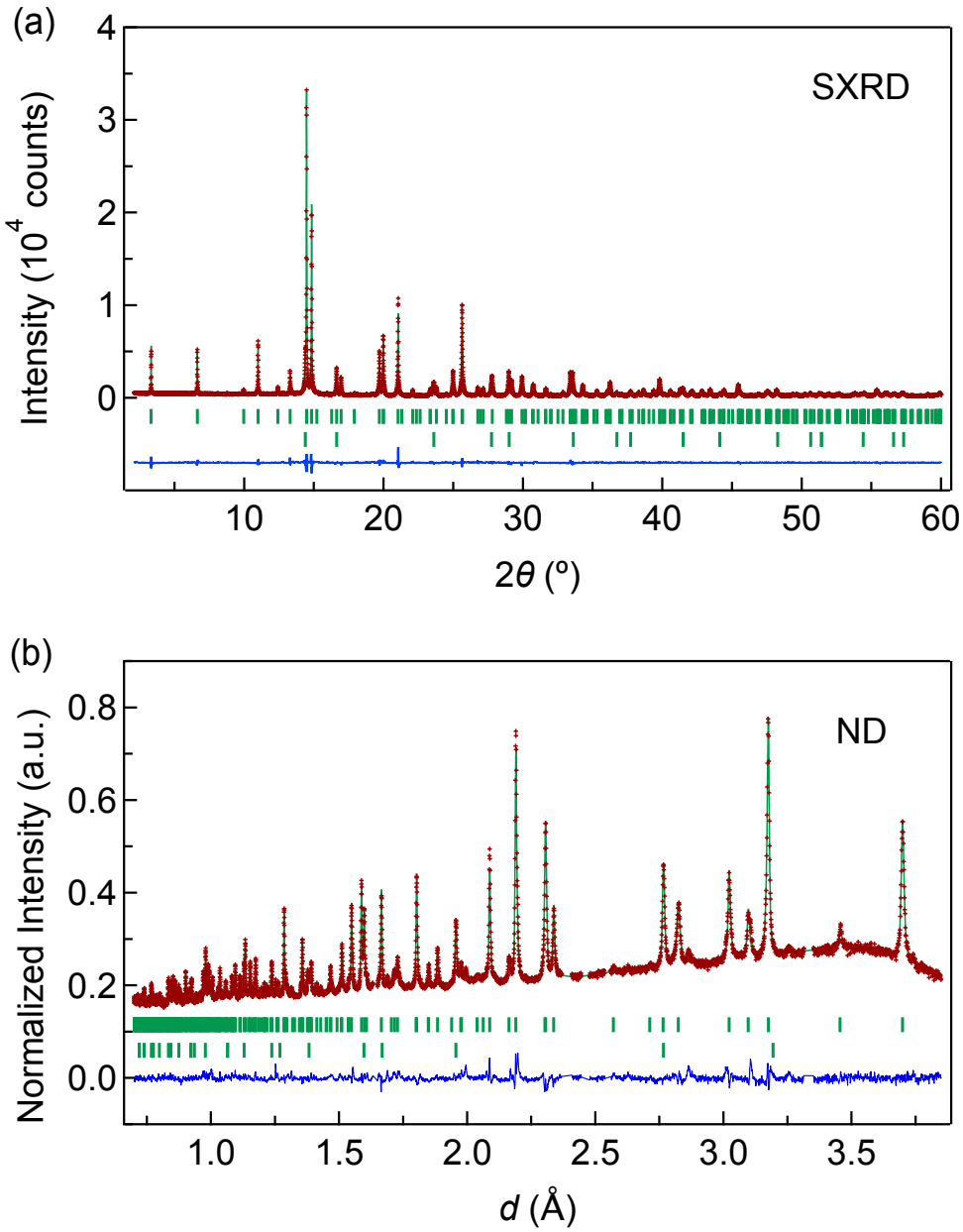

Figure 4.2 Observed and calculated (a) SXRD and (b) ND profiles for Ba_2YHO_3 at room temperature. Red crosses, green solid lines, and blue solid lines represent observed, calculated, and difference intensities, respectively. Upper and lower green ticks indicate the peak positions of Ba_2YHO_3 and BaO.

Table 4.1. Structural parameters of Ba_2YHO_3 from ND data collected at room temperature.

atom	site	*g*	*x*	*y*	*z*	*B* /Å^2
Ba(1)	2*c*	1	0.25	0.25	0.37573(8)	0.44(2)
Ba(2)	2*c*	1	0.25	0.25	0.10125(8)	0.44(2)
Y	2*c*	1	0.25	0.25	0.23708(7)	0.511(17)
H	2*c*	1	0.75	0.75	0.42303(16)	1.47(4)
O(1)	2*c*	1	0.75	0.75	0.08060(10)	1.42(2)
O(2)	4*f*	1	0.75	0.25	0.25826(6)	1.153(17)

*P*4/*nmm*; a = 4.380184(15) Å, c = 13.82378(8) Å.

R_{wp} = 2.78%, R_p = 2.06%, R_e = 0.86%, S = 3.21, R_B = 9.59%, R_F = 9.63%.

The XRD profile of the tetragonal phase was similar to that of K_2NiF_4-type oxyhydride Ba_2ScHO_3 (space group *I*4/*mmm*; No. 139), while the absence of extinctions, such as 00*l*, indicated a lowered symmetry. As shown in Figure 4.2, the powder synchrotron XRD (SXRD) and neutron diffraction (ND) profiles measured at room temperature were readily indexable with a unit cell of space group *P*4/*nmm* (No. 129) with lattice constants of a = 4.38035(3) Å and c = 13.82338(10) Å for SXRD and a = 4.380184(15) Å and c = 13.82378(8) Å for ND. Such a lowered symmetry from *I*4/*mmm* to *P*4/*nmm* in K_2NiF_4-type structures gives two non-equivalent apical sites (3/4 3/4 *z*), as reported in oxychlorides of Sr_2MO_3Cl (M = Fe, Co, Ni) wherein a quasi-square pyramidal MO_5 coordination is formed by O^{2-}/Cl^- anion ordering at the apical sites[26-28]. In addition, the vacancy formation is generally unfavourable in high pressure synthesis as seen in several oxyhydrides such as $LaSrMnO_{3.3}H_{0.7}$[29] and $BaScO_2H$[30]. We thus performed Rietveld analysis with assuming initial structural model based on the oxychlorides with a chemical formula of Ba_2YHO_3, wherein the Cl site was fully occupied by hydride ions. Refinement using ND data converged reasonably as shown in Figure 4.2b with agreement indexes of R_{wp} = 2.78% and R_p = 2.06%; the refined parameters are summarized in Table 1. Refinement using SXRD data, which assumed no hydrogen atoms, also converged (Figure 4.2a, R_{wp} = 7.26% and R_p = 5.52%, the refined parameters are in Table 4.1). Note that, when Na atoms were partially substituted with Ba or/and Y, the occupancy resulted in very small (< 0.02) or negative values, indicating that the amount of Na atoms was negligible within the lattice. Thermogravimetric analysis (TGA) under flowing Ar gas showed no weight loss up to 400 °C (Figure 4.3), which implies no significant change in the composition with annealing under ambient pressure.

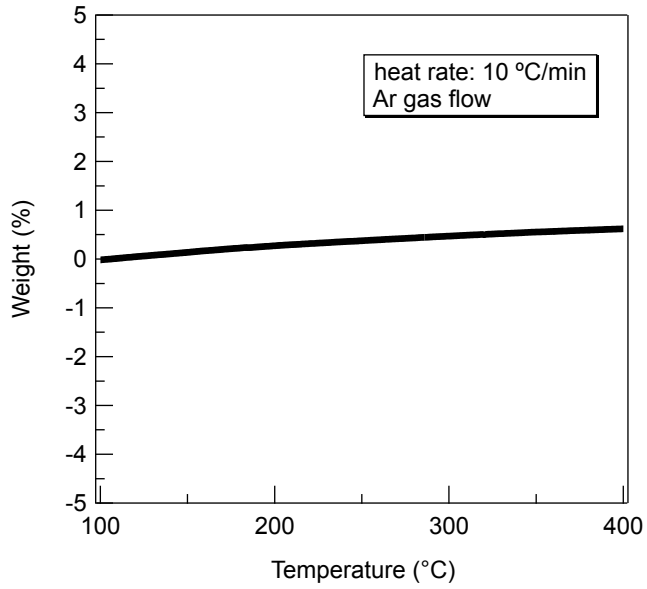

Figure 4.3 Thermogravimetric analysis (TGA) of Ba_2YHO_3 in heating under flowing Ar gas. The weight loss corresponding to hydrogen loss was not observed.

4.3.2 First principles calculations

Ba_2YHO_3 is the first case of layered perovskite oxyhydrides with the hydrogen-rich [Ba_2H_2] rock-salt layers. The quasi-pyramidal YO_5 coordination in the structure is in contrast with the octahedral ScH_2O_4 coordination in Ba_2ScHO_3 which has H^-/O^{2-} disordered rock-salt layers (Figure 4.1). For further insight into the anion arrangement, we performed first-principles calculations. Using a 2 × 2 × 1 supercell for Ba_2YHO_3, we determined by our calculations that a completely ordered arrangement was the most stable and found other metastable arrangements with H^-/O^{2-} disordering (Figure 4.4). Similar calculation results were also obtained for Ba_2ScHO_3,[10] wherein the proposed most stable arrangement with ordered [Ba_2H_2] and [Ba_2O_2] rock-salt layers was comparable in energy to other metastable arrangements with the H^-/O^{2-} disordering. To compare the Y and Sc cases, we focused on the energy difference (ΔE) between the most stable and metastable arrangements. Within the same energy range, the number of metastable arrangements of Ba_2YHO_3 was smaller than that of Ba_2ScHO_3 (Table 2). This result suggested that the ordered arrangement of Ba_2YHO_3 is formed more favorably than the other metastable arrangements.

The difference in structural symmetry could be discussed in terms of the Goldschmidt tolerance factor *t* for aristotype perovskites[31] such as the hypothetical “

$BaYO_2H$" and reported $BaScO_2H$[30]; this factor is defined as $t = (r_{Ba} + r_{H/O})/[\sqrt{2}(r_B + r_{H/O})]$) where r_{Ba}, r_B, and $r_{H/O}$ denote the ionic radii for Ba, B (= Sc, Y), and H/O, respectively, assuming that H^- and $O2^-$ are equal in size. Using the Shannon ionic radii[32], we obtained t = 0.925 for "$BaYO_2H$", which was smaller than that of $BaScO_2H$ (0.992). The larger deviation from unity, i.e. larger geometric distortion, for "$BaYO_2H$" would be responsible for the lowered symmetry of the Y coordination in Ba_2YHO_3. In mixed anion compounds, to tolerate the mismatch in ionic size, lowered symmetry is easily achieved by ordered heteroleptic coordination units, rather than rotations and tilts of rigid octhedra.

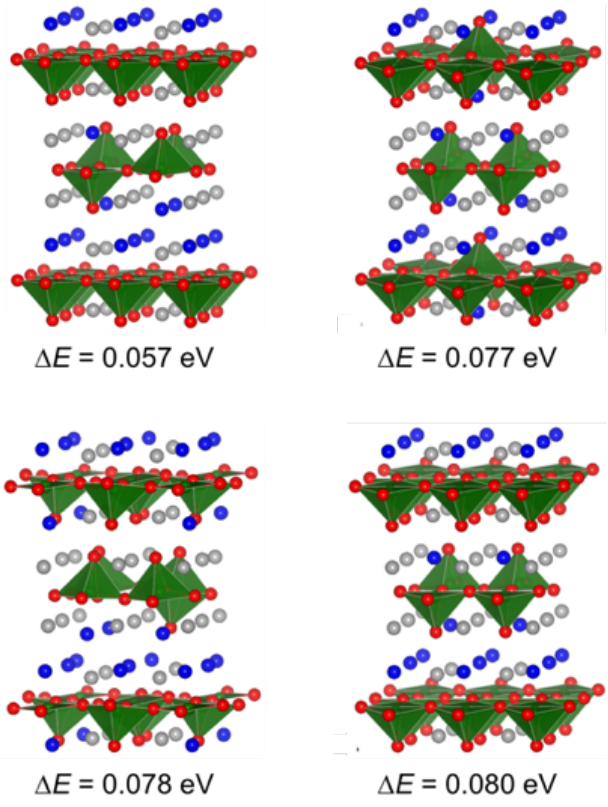

Figure 4.4 Representative metastable (ΔE < 0.1 eV/f.u.) arrangements for a 2 × 2 × 1 supercell of Ba_2YHO_3 obtained by first-principles calculations. The most stable arrangement was identical to the refined arrangement shown in Figure 4.1b.

Table 4.2 The number of metastable arrangements of Ba_2ScHO_3 and Ba_2YHO_3 within the range determined by the energy difference between the most stable and metastable arrangements

ΔE	Ba_2ScHO_3	Ba_2YHO_3
< 0.04	2	1
< 0.06	3	2
< 0.08	11	4
< 0.10	16	11

4.3.3 Ionic conductivity

Ionic conductivity of Ba_2YHO_3 was evaluated by the electrochemical impedance spectroscopy (EIS) using the as-synthesized pellet with sputtered Mo blocking electrodes. The measurements were done with heating and cooling at 160−400 °C under H_2 gas flow. The contribution of the impurity phases could be considered as negligible especially in bulk conduction, since BaO exhibits no ionic conduction and the amount of unreacted Na-species was insignificant (< 0.6 wt% in the mixture). The obtained Cole-Cole plots were separated into three regions: a semicircle in high frequency range, a broad small semicircle in middle frequency range, and a spike at low frequency range, which corresponded to responses from bulk, grain boundary, and electrode resistances, respectively (Figure 4.5a). We fitted the obtained data using an equivalent circuit model, and the temperature dependence of the total (bulk + grain boundary) conductivity was plotted in Figure 4.5b. The bulk conductivity data is shown in Figure 4.5(c&d). Similar conduction properties during heating and cooling indicated that Ba_2YHO_3 was stable throughout the measurements; this observation was supported by the fact that the *P*4/*nmm* symmetry was maintained in the XRD profiles after the EIS measurements (Figure 4.6). DC polarization measurement at 320 °C gave an electrical ($e^- + h^+$) conductivity of 7.86×10^{-8} $S \cdot cm^{-1}$, that can be ignored compared to the conductivity estimated from the EIS. The ionic transport number was calculated to be >99.5%, indicating that Ba_2YHO_3 is an ionic conductor without the contribution of e^- and h^+ conduction.

In the Li-based K_2NiF_4-type oxyhydrides (e.g., La_2LiHO_3), pure H^- conduction was confirmed in not only electrochemical experiments including solid state battery[6] and concentration cell tests[33], but also in first principles calculations wherein the migration energy of H^- is significantly smaller than that of O^{2-}[34,35]. In addition,

calculations for Ba_2ScHO_3 gave the much smaller defect formation and migration energies for H^- (~1.17 eV) compared to those for O^{2-} (~2.28 eV), indicating the pure H^- conduction in the rock salt layers[14]. Considering these facts, we determined that H^- ions are dominant charge carriers, while migration of divalent and hard O^{2-} ions should be much slow or none.

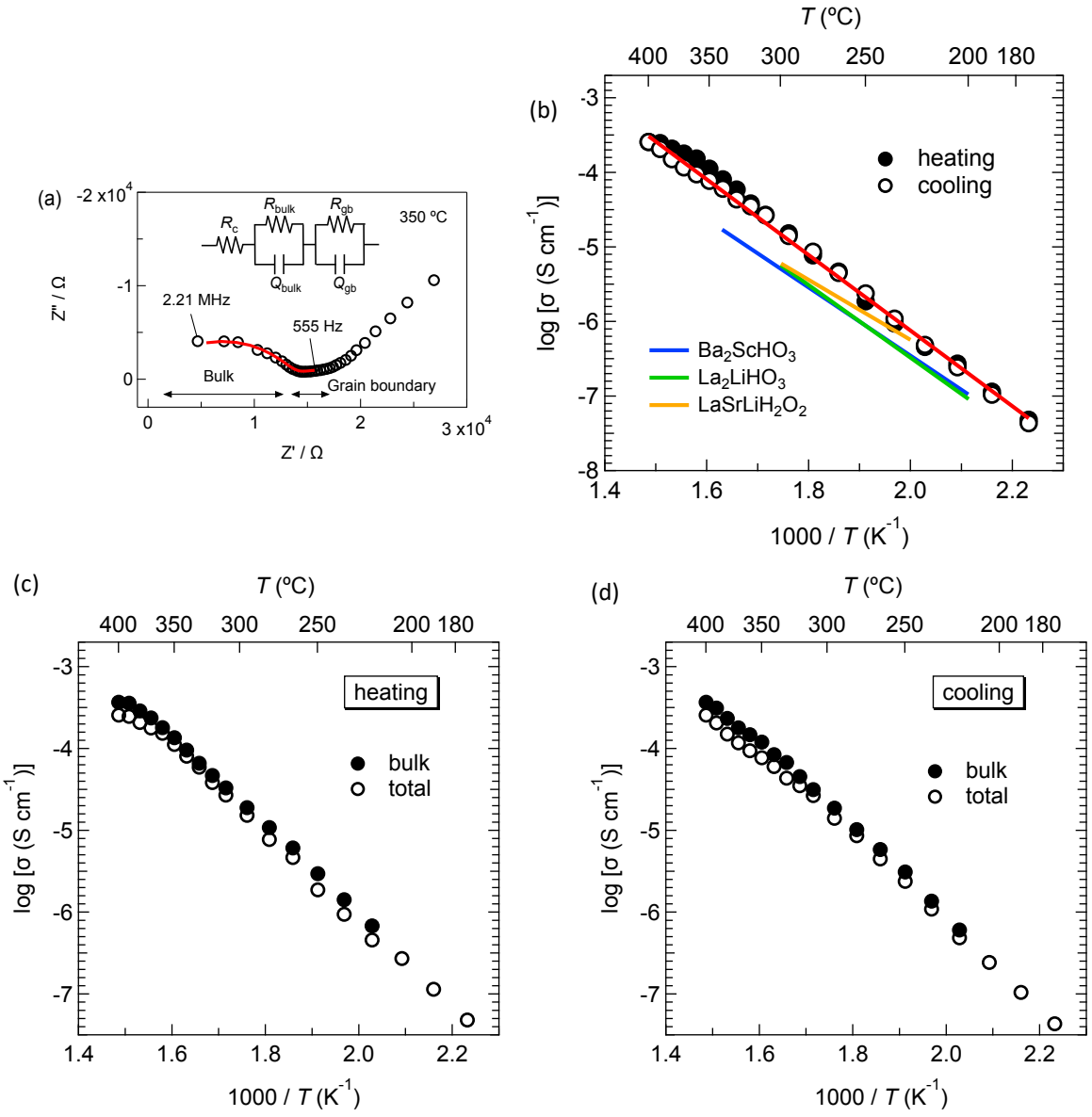

Figure 4.5 (a) Cole-Cole plot of Ba_2YHO_3 recorded at 350 °C. (b) Arrhenius plots of the total conductivity of Ba_2YHO_3 during heating (closed circles) and cooling (open circles); the linear fitting (red line) gives the activation energy range of 97.1–101 kJ·mol^{-1}. The blue, green, and orange lines represent the conductivities of Ba_2ScHO_3,[10] La_2LiHO_3, and $LaSrLiH_2O_2$,[6] respectively, Arrhenius plots of the bulk and total (bulk + grain boundary) conductivity of

Ba_2YHO_3 in (c) heating and (d) cooling.

The observed conductivity (s_H) of Ba_2YHO_3 was nearly five times higher than that of Ba_2ScHO_3 with anion-disordered rock-salt layers[10], and reached c.a. 1×10^{-4} S·cm^{-1} around 350 ºC. The higher conductivity could be attributed to an increase of actual carrier concentration in the rock-salt layers. In the anion-disordered [Ba_2HO] layers in Ba_2ScHO_3, local oxygen-rich regions with immobile O^{2-} contamination into the diffusion path would decrease long-range H^- diffusion probability. Inhibition of H^- diffusion by O^{2-} was also proposed in calculation study on $La_{2-x-y}Sr_{x+y}LiH_{1-x+y}O_{3-y}$[23], and the similar tendency is generally well known in layered rock-salt LiMO$_2$ (M = transition metal) where Li/M site-mixing drastically decreases the Li^+ diffusion[36]. In contrast, the completely anion-ordered [Ba_2H_2] layers in "ideal" Ba_2YHO_3 contain no O^{2-} contamination, and in actual should be more robust to possible site mixing.

The activation energy (E_a) of Ba_2YHO_3 at 175-350 °C was estimated as 1.08 eV that is slightly higher than that of Ba_2ScHO_3 (0.92 eV), in spite of the shorter nearest neighbour H-H path of 3.75786(14) Å (*vs.* 3.83 Å). Our previous computational study for Ba_2ScHO_3 has indicated that hydride ions diffuse through the rock-salt layer by means of vacancies and/or interstitialcy mechanisms[14]; the former is direct H-H hopping at apical sites through vacancies; the latter is a cooperative migration process that an interstitial H^- moves toward a neighboring apical site and the H^- originally located at the site moves to other interstitial sites. Given there are a suitable jump distance and bottleneck size for each conduction mechanism, the differences in the H^- coordination environment of Ba_2YHO_3 and Ba_2ScHO_3 might have slightly affected the activation energies. One could find a decrease in the slope of the Arrhenius plot of Ba_2YHO_3 at 350-400 °C (E_a = 0.59 eV), possibly implying that the interstitialcy mechanism with the lowest migration energy[14] may be dominant in the high temperature region. This result suggests that introducing excess H^- into the interstitial sites in Ba_2YHO_3 might be effective in improving the H^- conduction property (both s_H and E_a), as in O^{2-}/e^- mixed conductors $Ln_2NiO_{4+\delta}$[11-13]. As shown in Figure 4.5b, the conductivity of Ba_2YHO_3 is also higher than those of Li-based oxyhydrides La_2LiHO_3 and $LaSrLiH_2O_2$ wherein H^- ions diffuse among perovskite layers via equatorial-site hopping[6] in spite of the higher activation energy. The rock-salt layer is advantageous for H^- conduction in terms of allowing multiple diffusion mechanisms, while it is disadvantageous for H^- conduction in terms of H^- jump distances

because the H-H length between apical sites is significantly longer than that of equatorial sites. Such contradictory features related to the H^- conductivity in Ba_2YHO_3 are possibly reflected in the higher conductivity and higher activation energy than those of Li-based oxyhydrides.

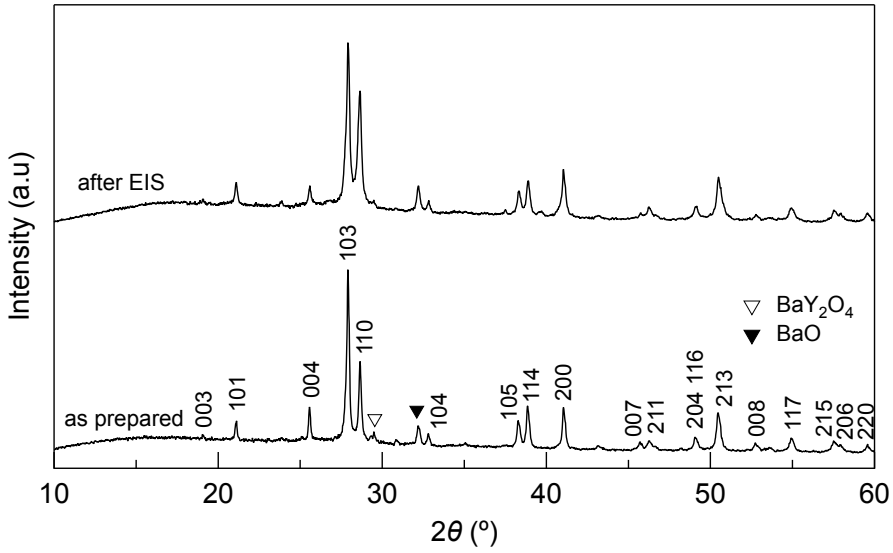

Figure 4.6 Laboratory XRD profiles of Ba_2YHO_3 before and after electrochemical impedance measurement.

4.4 Conclusion

In conclusion, we synthesized a new layered perovskite oxyhydride Ba_2YHO_3 as the first example containing hydrogen-rich $[Ba_2H_2]$ rock-salt layers. The H^- conductivity was higher than that of isostructural Ba_2ScHO_3 with anion-disordered $[Ba_2HO]$ layers due to the absence of immobile O^{2-} ions lying in the diffusion pathway. Detailed mechanism of H^- diffusion within rock-salt layers including relatively high activation energy compared to that within perovskite layers and/or decrease in the activation energy above 350 °C will be solved by further experiments such as maximum entropy method (MEM) analysis using high temperature ND data.

References

[1] Takahashi, T.; Kuwabara, K.; Shibata, M. Solid-state ionics - conductivities of Na^+ ion conductors based on NASICON. *Solid State Ionics* **1980**, 1, 163-175.

[2] Kamaya, N.; Homma, K.; Yamakawa, Y.; Hirayama, M.; Kanno, R.; Yonemura, M.; Kamiyama, T.; Kato, Y.; Hama, S.; Kawamoto, K.; Mitsui, A. A lithium superionic conductor. *Nat. Mat.* **2011**, 10, 682–686.G.

[3] Kanno, R.; Nakamura, S.; Ohno, K.; Kawamoto, Y. Ionic Conductivity of Tetragonal $PbSnF_4$ Prepared by Solid State Reaction in HF Atmosphere. *Mat. Res. Bull.* **1991**, 26 (11), 1111–1117.

[4] Kanno, R.; Ohno, K.; Izumi, H.; Kawamoto, Y.; Kamiyama, T.; Asano, H.; Izumi, F. Neutron Diffraction Study of the High-Fluoride-Ion Conductor, $PbSnF_4$, Prepared under an HF Atmosphere. *Solid State Ionics.* **1994**, 70–71, 253–258.

[5] Dénès, G.; Milova, G.; Madamba, M. C.; Perfiliev, M. Structure and ionic transport of $PbSnF_4$ superionic conductor. *Solid State Ionics* **1996**, 86-88, 77-82.

[6] Kobayashi, G.; Hinuma, Y.; Matsuoka, S.; Watanabe, A.; Iqbal, M.; Hirayama, M.; Yonemura, M.; Kamiyama, T.; Tanaka, I.; Kanno, R. Pure H^- conduction in oxyhydrides. *Science* **2016**, 351, 1314–1317.

[7] Iwasaki, Y.; Matsui, N.; Suzuki, K.; Hinuma, Y.; Yonemura, M.; Kobayashi, G.; Hirayama, M.; Tanaka, I.; Kanno, R. Synthesis, crystal structure, and ionic conductivity of hydride ion-conducting Ln_2LiHO_3 (Ln = La, Pr, Nd) oxyhydrides *J. Mat. Chem. A* **2018**, 6, 23457–23463.

[8] Ubukata, H.; Broux, T.; Takeiri, F.; Shitara, K.; Yamashita, H.; Kuwabara, A.; Kobayashi, G.; Kageyama, H. Hydride Conductivity in an Anion-Ordered Fluorite Structure LnHO with an Enlarged Bottleneck. *Chem. Mater.* **2019**. 31, 7360-7366.

[9] Fukui, K.; Iimura, S.; Tada, T.; Fujitsu, S.; Sasase, M.; Tamatsukuri, H.; Honda, T.; Ikeda, K.; Otomo, T.; Hosono, H. Characteristic fast H− ion conduction in oxygen-substituted lanthanum hydride. *Nat. Commun.* **2019**, 10, 2578.

[10] Takeiri, F.; Watanabe, A.; Kuwabara, A.; Nawaz, H.; Ayu, N. I. P.; Yonemura, M.; Kanno, R.; Kobayashi, G.; Ba_2ScHO_3: H^- conductive layered oxyhydride with H^- site selectivity. *Inorg. Chem*. **2019**, 58, 4431-4436.

[11] Skinner, S. J.; Kilner, J. A. Characterisation of $La_2NiO_{4+\delta}$ using in-situ high temperature neutron powder diffraction. *Solid State Ionics*. **2000**, 135, 709-712.

[12] Bassat, J. M.; Odier, P.; Villesuzanne, A.; Marin, C.; Pouchard, M. Anisotropic ionic transport properties in $La_2NiO_{4+\delta}$ single crystals. *Solid State Ionics*. **2004**, 167, 341-347.

[13] Yashima, M.; Enoki, M.; Wakita, T.; Ali, R.; Matsushita, Y.; Izumi, F.; Ishihara, T. Structural disorder and diffusional pathway of oxide ions in a doped Pr_2NiO_4-based mixed conductor. *J. Am. Chem. Soc.* **2008**, *130* (9), 2762–2763.

[14] Kuwabara, A.; Takeiri, F.; Nawaz, H.; Kobayashi, G. First-principles calculations of point defect formation and anion diffusion mechanism in oxyhydride Ba_2ScHO_3. **2020**, *ChemRxiv*, 10.26434/chemrxiv.12121254.v1.

[15] Izumi, F.; Momma, K. Three-Dimensional Visualization in Powder Diffraction. *Solid State Phenom*. **2007**, 130, 15−20.

[16] Oishi, R.; Yonemura, M.; Nishimaki, Y.; Torii, S.; Hoshikawa, A.; Ishigaki, T.; Morishima, T.; Mori, K.; Kamiyama, T. Rietveld analysis software for J-PARC. *Nucl. Instrum. Methods Phys. Res., Sect*. A **2009**, 600, 94−96.

[17] Momma, K.; Izumi, F. VESTA 3 for three-dimensional visualization of crystal, volumetric and morphology data. *J. Appl. Crystallogr*. **2011**, 44, 1272−1276.

[18] Blöchl, P. E. Projector augmented-wave method. *Phys. Rev. B*: *Condens. Matter Mater. Phys.* **1994**, 50, 17953−17979.

[19] Kresse, G.; Joubert, D. From ultrasoft pseudopotentials to the projector augmented-wave method. *Phys. Rev. B: Condens. Matter Mater. Phys.* **1999**, 59, 1758−1775.

[20] Kresse, G.; Hafner, J. Ab initio molecular dynamics for liquid metals. *Phys. Rev. B: Condens. Matter Mater. Phys*. **1993**, 47, 558−561.

[21] Kresse, G.; Furthmüller, J. Efficient iterative schemes for ab initio total-energy calculations using a plane-wave basis set. *Phys. Rev. B: Condens. Matter Mater. Phys*. **1996**, 54, 11169−11186.

[22] Kresse, G.; Furthmüller, J. Efficiency of ab-initio total energy calculations for metals and semiconductors using a plane-wave basis set. *Comput. Mater*. *Sci*. **1996**, 6, 15−50.

[23] Perdew, J. P.; Burke, K.; Ernzerhof, M. Generalized Gradient Approximation Made Simple. *Phys. Rev. Lett*. **1996**, 77, 3865−3868.

[24] Togo, A.; Tanaka, I. Spglib: a software library for crystal symmetry search. arXiv:1808.01590; **2018**.

[25] Monkhorst, H. J.; Pack, J. D. Special points for Brillouin-zone integrations. *Phys. Rev. B* **1976**, 13, 5188−5192.

[26] Tsujimoto, Y.; Yamaura, K.; Uchikoshi, T. Extended Ni(III) Oxyhalide Perovskite Derivatives: Sr_2NiO_3X (X = F, Cl). *Inorg. Chem.* **2013,** 52, 10211-10216.

[27] Loureiro, S. M.; Felser, C.; Huang, Q.; Cava, R. J. Refinement of the crystal structures of strontium cobalt oxychlorides by neutron powder diffraction. *Chem. Mater*. **2000**, 12, 3181-3185.

[28] Hector, A. L.; Hutchings, J. A.; Needs, R. L.; Thomas, M. F.; Weller, M. T. Structural and Mössbauer study of Sr_2FeO_3X (X = F, Cl, Br) and the magnetic structure of Sr_2FeO_3F. *J. Mater. Chem.* **2001**, 11, 527-532.

[29] Tassel, C.; Goto, Y.; Watabe, D.; Tang, Y.; Lu, H.; Kuno, Y.; Takeiri, F.; Yamamoto, T.; Brown, C. M.; Hester, J.; Kobayashi, Y.; Kageyama, H. High-pressure synthesis of manganese oxyhydride with partial anion order. *Angew. Chem.* **2016**, 128, 9819–9822.

[30] Goto, Y.; Tassel, C.; Noda, Y.; Hernandez, O.; Pickard, C. J.; Green, M. A.; Sakaebe, H.; Taguchi, N.; Uchimoto, Y.; Kobayashi, Y.; Kageyama, H. Pressure-Stabilized Cubic Perovskite Oxyhydride $BaScO_2H$. *Inorg. Chem.* **2017,** 56, 4840-4845.

[31] Goldschmidt, V. M. Die Gesetze der Krystallochemie. *Naturwissenschaften* **1926**, 14, 477–485.

[32] Shannon, R. T. Revised effective ionic radii and systematic studies of interatomic distances in halides and chalcogenides. *Acta crystallographica section A: crystal physics, diffraction, theoretical and general crystallography.* **1976**, 32, 751-767.

[33] Matsui, N.; Kobayashi, G.; Suzuki, K.; Watanabe, A.; Kubota, A.; Iwasaki, Y.; Yonemura, M.; Hirayama, M.; Kanno, R. Ambient pressure synthesis of la_2liho_3 as a solid electrolyte for a hydrogen electrochemical cell. *J. Am. Ceram. Soc.* **2019**, 102, 3228-3235.

[34] Liu, X.; Bjørheim, T. S.; Haugsrud, R. Formation of defects and their effects on hydride ion transport properties in a series of K_2NiF_4 -type oxyhydrides. *J. Mat. Chem. A*. **2018**, *6* (4), 1454–1461.

[35] Bai, Q.; He, X.; Zhu, Y.; Mo, Y. First-principles study of oxyhydride H^- ion conductors: toward facile anion conduction in oxide-based materials. *ACS Applied Energy Materials.* **2018**, 1 (4), 1626–1634.

[36] Whittingham, M. S. Ultimate Limits to Intercalation Reactions for Lithium Batteries. *Chem. Rev.* **2004**, 114(23), 4271-4302.

Chapter 5

Summary

Hydride (H^-) is an anionic specie with attractive characteristics for fast conduction, e.g. monovalence, suitable size, and large polarizability. Irvine *et al.* showed a significant H^- conductivity of 0.2 S cm^{-1} at 630 °C in metal hydride BaH_2.[1] Kobayashi *et al*. reported hydride conduction in Li-based oxyhydride series $La_{2-x-y}Sr_{x+y}LiH_{1-x+y}O_{3-y}$ ($0 \leq x \leq 1$, $0 \leq y \leq 2$) with layered perovskite (K_2NiF_4-type) structures.[2] Design of materials with anion sublattices having preferred occupation is crucial for fast hydride ion conduction , since less mobile oxide ions inhibit hydride conduction. Nevertheless, the "immobile" ions facilitate the conduction process by forming the crystal frameworks with suitable diffusion pathways for conduction of the mobile ions. Compared to anionic conductors which are single-anion systems, this phenomenon is prevalent in some cationic conductors with multiple cations such as NASICON[3] and LGPS.[4] Since recently, some oxyhydrides have shown excellent hydride ion conductivities,[2,5] the current study focused on exploring these mixed anion systems as anion conductors to study the effect of mobile H^- and immobile O^{2-} ions towards design of anionic sublattices and eventually ion conduction properties.

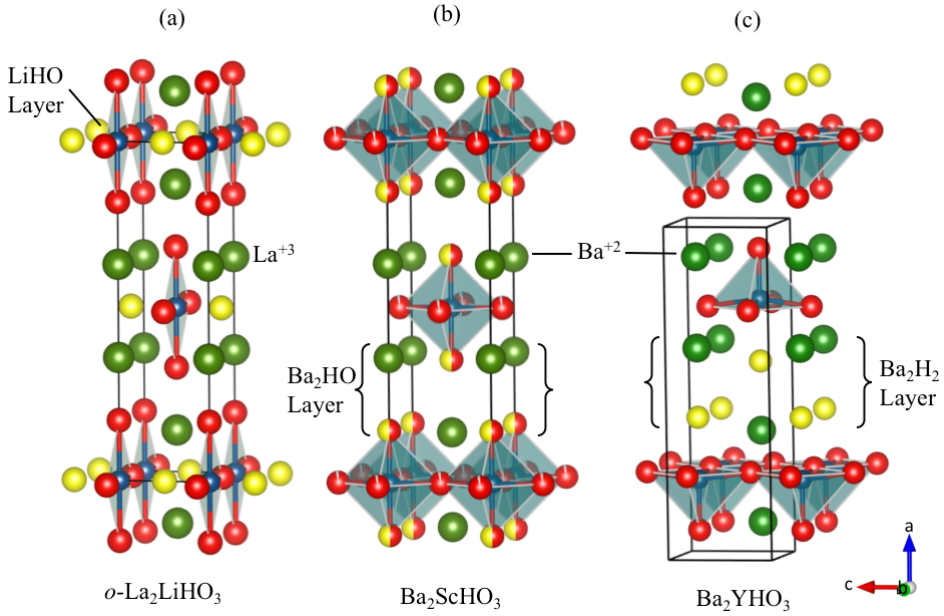

Figure 5.1 Crystal structures of (a) La_2LiHO_3, (b) Ba_2ScHO_3 and (c) Ba_2YHO_3 showing different anionic arrangements

Chapter 3 described a new oxyhydride Ba_2ScHO_3[6] which adopts the K_2NiF_4-type structure with preferred apical H^- ions. Several reports indicated evidences of fast O^{2-} conduction in isostructural $Ln_2NiO_{4+\delta}$ where interstitial anion sites contribute to conduction.[7,8] First principal calculations regarding point defect formation and conduction mechanism revealed hydride ions as predominant charge carriers.[9] The Sc based oxyhydride showed a superior H^- ion conductivity to that of an ideal perovskite $BaScO_2H$. The as shown non-dependence of conductivity on H_2/Ar towards EIS measurement revealed absence of any electronic conduction. In comparison to La_2LiHO_3 with similar carrier concentration, the conductivity of the two oxyhydrides despite different conduction pathways was not much different. This could be due to the co-occupancy of larger immobile O^{2-} ions at the same sites which partially impeded the conduction path way.

In chapter 4, we reported a new H^- conductive oxyhydride Ba_2YHO_3, which adopted a K_2NiF_4-type structure with complete H^-/O^{2-} anion ordering to form $[Ba_2H_2]$ rock-salt layers. Such a hydride ion ordering lowered the symmetry of this *Y* based oxyhydride to *P*4/*nmm* as compared to its predecessor Ba_2ScHO_3 which crystallized in high symmetry *I*4/*mmm* space group as indicated by the structural analysis by both SXRD and ND data. First principles calculations also outlined the higher stability of the structure with complete ordering as compared to other metastable structures. The H^- conductivity sought a considerable improvement(Figure 5.2) in comparison to both La_2LiHO_3 and Ba_2ScHO_3 which have [LiHO] and $[Ba_2HO]$ diffusion layers respectively. [10]

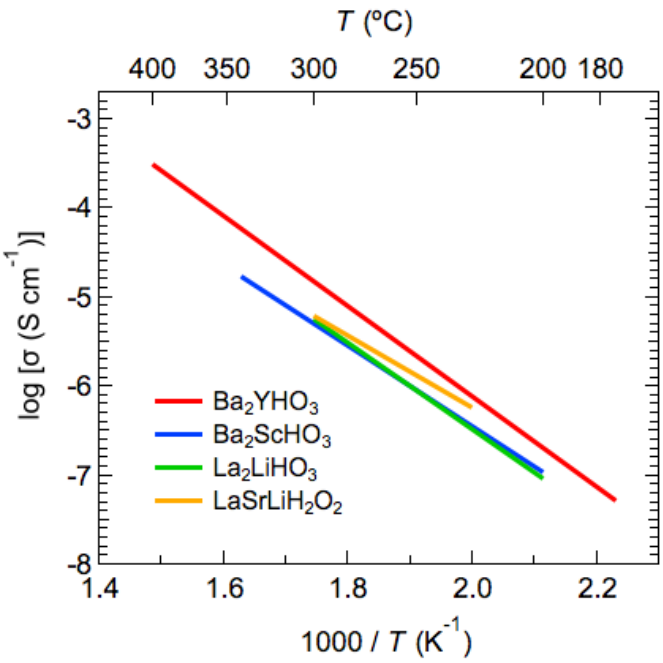

Figure 5.0-1 Arrhenius plot of ionic conductivities of Ba_2YHO_3 in comparison with La_2LiHO_3, $LaSrLiH_2O_2$ and Ba_2ScHO_3

Layered oxyhydride are composed of alternate stacks of perovskite and rock salt layers where both layers are capable of ionic diffusion separately. Previously in LSLHO oxyhydrides, the conduction occurred dominantly through perovskite layers as indicated by the theoretical calculations.[11] Current study of rock salt ordered Sc and Y based oxyhydrides helped to validate the idea of tuning the site selectivity of H^- according to the electrostatic valence rule and potential of rock salt layers in order to design the H^- diffusion pathway in layered oxyhydrides. The study revealed that within the rock salt layers, anion order/disorder plays a crucial role for smooth hydride ions diffusion. The anion disorder at apical sites in Ba_2ScHO_3 prevented the facile diffusion of hydride ions through Ba_2HO rock salt layers. Consideration of larger Y cation at B site with tolerance factor further away from unity helped to form a K_2NiF_4-type structure with lowered symmetry resulting in a complete rock salt ordering to form hydride rich Ba_2H_2 layers. As a result, the hydride ion conductivity of Ba_2YHO_3 enhanced five times as compared to its predecessor Ba_2ScHO_3. The Sc and Y based layers oxyhydride based compositions can be fine-tuned by introduction of vacancies or the addition of hydrogen into the interstitial sites within the layer to further optimize the conductivity.

References

[1] Verbraeken, M. C.; Cheung, C.; Suard, E.; Irvine, J. T. High H^- ionic conductivity in barium hydride. *Nat Mater* **2015,** 14, 95-100.

[2] Kobayashi, G.; Hinuma, Y.; Matsuoka, S.; Watanabe, A.; Iqbal, M.; Hirayama, M.; Yonemura, M.; Kamiyama, T.; Tanaka, I.; Kanno, R. Pure H^- conduction in oxyhydrides. *Science* **2016,** 351, 1314-1317.

[3] Takahashi, T.; Kuwabara, K.; Shibata, M. Solid-state ionics - conductivities of Na^+ ion conductors based on NASICON. *Solid State Ionics* **1980**, 1, 163-175.

[4] Kamaya, N.; Homma, K.; Yamakawa, Y.; Hirayama, M.; Kanno, R.; Yonemura, M.; Kamiyama, T.; Kato, Y.; Hama, S.; Kawamoto, K.; Mitsui, A. A lithium superionic conductor. *Nat. Mat.* **2011**, 10, 682–686.G.

[5] Iwasaki, Y.; Matsui, N.; Suzuki, K.; Hinuma, Y.; Yonemura, M.; Kobayashi, G.; Hirayama, M.; Tanaka, I.; Kanno, R. Synthesis, crystal structure, and ionic conductivity of hydride ion-conducting Ln_2LiHO_3 (Ln = La, Pr, Nd) oxyhydrides *J. Mat. Chem. A* **2018**, 6, 23457–23463.

[6] Takeiri, F.; Watanabe, A.; Kuwabara, A.; Nawaz, H.; Ayu, N. I. P.; Yonemura, M.; Kanno, R.; Kobayashi, G.; Ba_2ScHO_3: H^- conductive layered oxyhydride with H^- site selectivity. *Inorg. Chem*. **2019**, 58, 4431-4436.

[7] Skinner, S. J.; Kilner, J. A. Characterisation of $La_2NiO_{4+\delta}$ using in-situ high temperature neutron powder diffraction. *Solid State Ionics*. **2000**, 135, 709-712.

[8] Lee, D.; Lee, H. N. Controlling oxygen mobility in ruddlesden–popper oxides. *Materials (Basel)* **2017**, 10. 368

[9] Kuwabara, A.; Takeiri, F.; Nawaz, H.; Kobayashi, G. First-principles calculations of point defect formation and anion diffusion mechanism in oxyhydride Ba_2ScHO_3. **2020**, *ChemRxiv*, 10.26434/chemrxiv.12121254.v1.

[10] Nawaz, H.; Takeiri, F.; Kuwabara, A.; Yonemura, M.; Kobayashi, G. Synthesis and H^- Conductivity of a New Oxyhydride Ba_2YHO_3 with Anion-Ordered Rock-Salt Layers. *Chem. Commun.* **2020**, *56* (71), 10373-10376.

[11] Fjellvåg, Ø. S.; Armstrong, J.; Vajeeston, P.; Sjåstad, A. O. New Insights into Hydride Bonding, Dynamics, and Migration in La_2LiHO_3 Oxyhydride. *J. Phys. Chem. Let.* **2018,** 9, 353-358.

List of Publications

Chapter 3

- Takeiri, F.; Watanabe, A.; Kuwabara, A.; Nawaz, H.; Ayu, N. I. P.; Yonemura, M.; Kanno, R.; Kobayashi, G.; Ba_2ScHO_3: H^- conductive layered oxyhydride with H^- site selectivity. *Inorg. Chem*. **2019**, 58, 4431-4436.

Chapter 4

- Nawaz, H.; Takeiri, F.; Kuwabara, A.; Yonemura, M.; Kobayashi, G. Synthesis and H^- Conductivity of a New Oxyhydride Ba_2YHO_3 with Anion-Ordered Rock-Salt Layers. *Chem. Commun.* **2020**, *56* (71), 10373-10376.

Collaborative work

- Kuwabara, A.; Takeiri, F.; Nawaz, H.; Kobayashi, G. First-principles calculations of point defect formation and anion diffusion mechanism in oxyhydride Ba_2ScHO_3. **2020**, *ChemRxiv*, 10.26434/chemrxiv.12121254.v1.

Acknowledgements

First and above all, I thank Allah Almighty to whom I owe my very existence for providing me this opportunity and granting me capability to proceed successfully.

I would like to express my sincere gratitude to my supervisor Associate Professor Genki Kobayashi for the continuous support during my Ph.D study and related research, for his patience, continuous motivation, and immense knowledge. His guidance helped me in all the time of research and writing of this thesis. I could not have imagined having a better advisor and mentor for my Ph.D study.

Besides my supervisor, I would like to thank Assistant Professor Fumitaka Takeiri for the valuable discussions and the continuous support in my research project and to prepare my thesis draft. My sincere thanks also go to Dr. Akihide Kuwabara at Japan Fine Ceramics Center for the collaborative work regarding theoretical calculations, Professor Takashi Kamiyama and Associate Professor Masao Yonemura at High Energy Accelerator Research Organization (KEK) for the neutron diffraction studies, without their precious support it would not be possible to conduct this research.

I gratefully acknowledge the contribution of Dr. Sara Qaisar, and Dr. Mohammad Shuaib at my parent institute National Center for Physics Islamabad for approval of my study leave for my doctoral studies and for the continuous moral support during this period. A very special thank you to Dr. Mohammad Iqbal for introducing me to my supervisor Dr. Genki Kobayashi and convincing me to pursue my doctoral studies in japan.

I am especially thankful to my ex lab mate Dr. Akihiro Watanabe for providing the initial guideline of my research project. I thank my fellow lab mates Ayu, Okamoto and Asad and visiting students for the stimulating discussions and for their supportive behavior during the experiments and for keeping the lab environment friendly. I also thank the technical staff in my lab Mr. Yamanaka, Mrs. Akiko Kubata, Mrs. Yumiko Imai and Mrs. Masako Nishikawa at Kobayashi lab IMS for their technical support. Also, I greatly appreciate the support from my house mates shenguanshuo and Ruan de Villiers and friends Iqbal, Mahesh, Misbah, Ken and Ohara for making my off-campus life cheerful during my stay in Japan.

Lastly, to my family, this PhD study would not have been possible without their cooperation and extended support, my wife Dr. Humaira Erum without whom, I would not have had the courage to embark on this journey in the first place and for her tireless support throughout writing this thesis and my life in general, my loving kids, my mother, for her countless prayers for my success and to my brothers and sister, specially my younger sister Rubina for the moral encouragement.